

Prion protein conversion at two distinct cellular sites precedes fibrillisation

Juan Ribes

UCL Institute of Prion Diseases <https://orcid.org/0000-0003-0363-3519>

Mitali Patel

UCL Institute of Prion Diseases <https://orcid.org/0000-0002-8098-2344>

Halim Halim

UCL Institute of Prion Diseases <https://orcid.org/0000-0002-3848-8449>

Sharon Tooze

The Francis Crick Institute <https://orcid.org/0000-0002-2182-3116>

Peter Kloehn (✉ p.kloehn@prion.ucl.ac.uk)

UCL Institute of Prion Diseases

Article

Keywords:

Posted Date: May 20th, 2022

DOI: <https://doi.org/10.21203/rs.3.rs-1622593/v1>

License:   This work is licensed under a Creative Commons Attribution 4.0 International License.

[Read Full License](#)

1 **Prion protein conversion at two distinct cellular sites precedes fibrillisation**

2 Juan Manuel Ribes^{1#}, Mitali P. Patel^{1#}, Hazim A. Halim¹, Sharon A. Tooze², Peter-Christian
3 Klöhn^{1*}

4 ¹Medical Research Council Prion Unit at UCL, Institute of Prion Diseases, University College
5 London, London W1W 7FF, United Kingdom

6 ²Molecular Cell Biology of Autophagy Laboratory, the Francis Crick Institute, London NW1
7 1BF, United Kingdom

8

9 # joint first authors

10

11

12

13

14

15

16

17

18 Correspondence: p.kloehn@prion.ucl.ac.uk

19

20

21 **Summary**

22 The self-templating nature of prions plays a central role in prion pathogenesis and is
23 associated with infectivity and transmissibility. Since propagation of proteopathic seeds has
24 now been acknowledged a principal pathogenic process in many types of dementia, more
25 insight into the molecular mechanism of prion replication is vital to delineate specific and
26 common disease pathways. By employing highly discriminatory anti-PrP antibodies and
27 conversion-tolerant PrP chimera, we here report that *de novo* PrP conversion and formation
28 of fibril-like PrP aggregates are distinct in mechanistic and kinetic terms. *De novo* PrP
29 conversion occurs within minutes after infection at two subcellular locations, while fibril-like
30 PrP aggregates are formed exclusively at the plasma membrane, hours after infection.
31 Phenotypically distinct pools of abnormal PrP at perinuclear sites and the plasma membrane
32 show differences in N-terminal processing, aggregation state and amyloid formation and are
33 linked by exocytic transport via synaptic and large-dense core vesicles.

34

35 **Introduction**

36 The “protein only hypothesis”¹ proposes that an abnormal conformer of PrP causes self-
37 templating protein aggregation by converting host-encoded cellular prion protein (PrP^c)²⁻⁴,
38 but the cellular mechanism of conversion has remained elusive. A major roadblock for the
39 study of self-templating protein aggregation in prion diseases is the lack of anti-PrP
40 antibodies that discriminate PrP^c from abnormal PrP, here termed disease-associated PrP
41 (PrP^d). Since the vast majority of anti-PrP antibodies characterised to date are non-
42 discriminatory or “pan” antibodies⁵, reliance on the enzymatic or chemical removal of PrP^c
43 has greatly limited progress in the investigation of PrP conversion.

44 Pivotal questions concerning the biology of PrP conversion have remained a matter of
45 controversy. Firstly, the cellular site of prion replication remains unsolved and putative sites
46 include the endocytic recycling pathway^{6, 7}, the endosomal-lysosomal pathway⁸⁻¹⁰, the Golgi
47 apparatus^{11, 12} and the plasma membrane^{13, 14}. Secondly, the kinetics of *de novo* PrP
48 conversion, a comparatively unexplored question in prion biology, is a matter of debate.
49 Evidence that PrP converts within minutes after infection¹³ has been disputed by others¹⁵,
50 who claim that proteinase K-resistant PrP (PrP^{Sc}) is not detectable before 24 hours after
51 infection, raising the question whether distinct oligomeric states of abnormal PrP aggregates
52 may explain these inconsistencies. Thirdly, early studies of prion-infected mice showed
53 evidence of “prion-amyloid filaments” in the extracellular space beneath the ependyma¹⁶ and
54 recent studies characterised *ex vivo* isolated prion rods^{17, 18}, but the formation and elongation
55 of prion rods has not been recapitulated in neuronal cells. A recent study reported the
56 detection of lipid raft-associated amyloid strings and webs of PrP, but the molecular mode of
57 amyloid formation is unknown¹⁴.

58 To address these current challenges, we identified highly discriminatory anti-PrP antibodies
59 and conversion-tolerant, tagged *Prnp* chimera to examine aggregation phenomena in freshly
60 and persistently prion-infected neuronal cells.

61 We provide evidence that (i) PrP conversion occurs within minutes after infection at two
62 distinct cellular sites and precedes the formation of nascent abnormal PrP conformers, (ii)
63 fibril-like PrP^d aggregates are formed and elongated at the plasma membrane, while
64 amyloidogenic fibrils are absent intracellularly, (iii) the prion infectious state is dependent on
65 functional dynamins and Cdc42, (iv) PrP^d segregates into synaptic and large-dense core
66 vesicles of the regulated secretory pathway.

67

68 Results

69 Phenotypically distinct PrP^d aggregates in prion-infected cells identified by 70 monospecific anti-PrP antibodies

71 To identify highly validated anti-PrP antibodies, we characterised 18 frequently used
72 monoclonal antibodies (mAbs) with respect to their target-specificity and propensity to
73 discriminate PrP^d from PrP^c (Fig. 1A). We deleted *Prnp* in N2a cells to unequivocally
74 demonstrate that mAbs are target-specific as shown for example for 5B2 and 6D11 (Fig.
75 1B). Seven mAbs were target-specific, also termed monospecific¹⁹, while 4 mAbs showed
76 moderate and 7 mAbs showed significant off-target effects (Fig. S1A and Table S1).
77 Validated mAbs used in this study recognise distinct PrP regions which include the N-
78 terminus (5B2, 8B4), the octapeptide repeat region (Saf32), charge cluster 2 (6D11), α -helix
79 1 (ICSM 18) and α -helix 2 (8H4; Fig. 1A).

80 Unexpectedly, monospecific mAbs showed phenotypic differences in single-labelled prion-
81 infected cells of the same culture (Fig. S1B-E). Fibril-like PrP^d aggregates were detected
82 with 5B2 at the extracellular matrix (ECM) in infected cells (Fig. S1B), while 6D11 labelling
83 revealed a punctuate staining predominantly at perinuclear regions (Fig. S1C). ICSM18
84 detected PrP^d aggregates at the ECM (Fig. S1D) and 8H4 labelled aggregates were
85 reminiscent of the punctate 6D11 phenotype (Fig. S1E). This finding prompted us to
86 investigate mAb-dependent differences of PrP^d phenotypes in more detail.

87 Fibril-like PrP^d aggregates are tethered to the plasma membrane and extend to the 88 ECM

89 Unless otherwise specified, all labelling experiments were conducted under denaturing
90 conditions, i.e. in presence of guanidinium thiocyanate (GTC), where the majority of anti-PrP
91 mAbs detect abnormal PrP^{5, 20, 21}. Prolonged cultures (≥ 6 days) of prion-infected cells
92 displayed extensive fibril-like 5B2-positive PrP^d aggregates that are tethered to the plasma
93 membrane and extend to the ECM (Fig. 1C, upper panel). To normalise the distance of focal
94 planes in z-direction, we used in-focus detection of the ECM-resident protein focal adhesion
95 kinase (FAK), arbitrarily denoted “zero μm ”, as focal reference level as elaborated in
96 Methods. Serial sections from the ECM to the focal plane of the nucleus demonstrate that
97 5B2 labelled PrP^d at the plasma membrane, while the cytosolic face of the cell remained
98 void with no 5B2-positive PrP^d detected intracellularly. In contrast, 6D11 labelled punctate
99 PrP^d aggregates at perinuclear sites, at the plasma membrane and extracellularly (Fig. 1C,
100 lower panel). Double-labelling experiments with 5B2 and 6D11 corroborate these phenotypic
101 differences. Whilst both antibodies colabelled PrP^d aggregates at the plasma membrane,
102 5B2 failed to detect perinuclear PrP^d (Fig. 1D). In uninfected control cells, both antibodies
103 weakly labelled the plasma membrane (Fig. 1E). In contrast to 5B2, mAbs against α -helix 1
104 (ICSM 18) and α -helix 2 (8H4) colabelled 6D11-positive PrP^d aggregates at perinuclear sites
105 as depicted in fluorescence intensity profiles (Fig. 1F). Double-labelled images for all
106 selected monospecific mAbs are shown in Fig. S2. While failure to label perinuclear PrP^d
107 with 5B2 is confirmed with the N-terminal mAb 8B4, all other mAbs labelled perinuclear PrP^d
108 aggregates.

109 To identify anti-PrP mAbs that best discriminate PrP^d from PrP^c, we quantified the relative
110 fluorescence intensities of mAbs in prion-infected and uninfected cells at all cellular
111 compartments where PrP^d is detected, i.e. the plasma membrane, perinuclear regions and
112 the ECM. Voxel-based fluorescence intensities in Fig. 1G are normalised and provide a
113 quantitative scale for their discriminatory propensities at the specified subcellular locations
114 (see Table S2 for data). Notably, at the plasma membrane, only 5B2 and 6D11 showed 10-

115 fold or higher fluorescence intensities in infected versus uninfected cells, while a more
116 intense PrP^c label with ICSM18, Saf32 and 8H4 limits their use to detect PrP^d at the plasma
117 membrane. All mAbs, except 8H4, were sufficiently discriminatory to call PrP^d at the ECM,
118 while low differential fluorescence intensities for ICSM18 limit its use in detecting PrP^d at
119 perinuclear regions.

120 Phenotypic differences between intracellular and extracellular PrP^d aggregates, detected
121 with 5B2 and 6D11, respectively are not limited to mouse neuroblastoma cell lines, as shown
122 in Fig. 1H. Primary neuronal cultures from embryonic e17 mouse brains, infected with 22L
123 prions showed 5B2-positive long fibril-like PrP^d aggregates at the cell periphery of GFAP-
124 positive astrocytes with 6D11-positive PrP^d puncta at perinuclear sites at three weeks post
125 infection (Fig. 1H), thus corroborating the phenotypic features of the mAb pair in
126 neuroblastoma cells.

127 **Elongation, average length and structural features of fibril-like PrP^d aggregates**

128 To characterise the time-dependence of PrP^d fibril elongation, we infected primary neuronal
129 cultures from brains of FVB wild-type (wt) and prion-replication deficient FVB *Prnp*^{-/-} mice
130 with the mouse RML prions. In cultures from FVB wt mouse brains, fibril length continuously
131 and significantly increased over three weeks, at mean fibril elongation rates of 190 nm per
132 day, reaching lengths of up to 15 µm, while no fibrils were detected at the periphery of
133 astrocytes from brains of FVB *Prnp*^{-/-} mice (Fig. 2A, B).

134 To investigate the phenotype of fibril-like PrP^d at subdiffraction resolution, we co-labelled
135 PrP^d at the ECM of prion-infected S7 (iS7) cells with 5B2 and 6D11 and imaged labelled
136 cells using structured illumination microscopy (SIM, Fig. 2C). Notably, extended segments of
137 PrP^d fibrils did not show co-labelling under denaturing conditions. Instead, 5B2 immuno-
138 positivity prevailed with 6D11-positive puncta along the lengths and at ends of fibrils. Where
139 6D11 puncta were detected in close proximity to 5B2-positive fibrils, areas of colocalisation
140 were apparent (see inserts in Fig. 2C). This result is consistent with the observed punctate
141 and fibril-like phenotype of PrP^d aggregates in single-labelled prion-infected cells (Fig. 1C)
142 and suggests (i) that different aggregation states may co-exist during PrP^d fibril formation
143 and (ii) that the charge cluster 2 region where 6D11 binds may be cryptic in highly ordered
144 amyloidogenic aggregates.

145 **Identification of conformational and truncated PrP^d variants in prion-infected cells**

146 While it is well documented that some anti-PrP mAbs that recognise PrP^c under native
147 conditions fail to detect PrP^d aggregates in prion-infected cells, unless cells are treated with
148 denaturing agents after fixation^{5, 20, 21}, this phenomenon has not been broadly investigated
149 with panels of validated anti-PrP mAbs. Our initial results show that prion-infected cells,
150 labelled with the monospecific core mAbs 6D11, ICSM18 and 8H4 in absence of GTC are
151 phenotypically indistinguishable from uninfected cells (Fig. S3), suggesting that those PrP
152 epitopes are cryptic under native conditions. This notion however does not explain why 5B2
153 fails to detect intracellular PrP^d under denaturing conditions (Fig. 1C, D and F).

154 We thus examined monospecific anti-PrP mAbs under native and denaturing conditions (Fig.
155 2D) at all sites of PrP^d deposits (Fig. S4). The binding characteristics of all investigated
156 mAbs are summarised in Fig. 2E. In keeping with the binding characteristics of 5B2 in Fig. 1,
157 all N-terminal mAbs detected fibril-like PrP^d at extracellular sites (ECM and plasma
158 membrane), but not intracellularly. MABs that bind to the “core” PrP region (90-231)²² failed
159 to detect PrP^d in prion-infected cells under native conditions, while PrP^d aggregates were
160 readily detected following denaturation. Saf32 showed notable propensities, in that it
161 detected extracellular fibril-like PrP^d under native conditions, like N-terminal mAbs and

162 intracellular PrP^d under denaturing conditions, unlike N-terminal mAbs, suggesting that
163 extracellular and intracellular PrP^d species are conformationally distinct at the octapeptide
164 repeat region (Fig. 2E and Fig. S4).

165 To investigate whether failure to detect intracellular PrP^d with N-terminal mAbs is due to
166 proteolytic processing, we tested whether an increase in the endosomal/lysosomal pH may
167 restore intracellular PrP^d labelling by 5B2. Activation of endosomal/lysosomal proteinases is
168 tightly regulated by the intraorganellar pH²³ and bafilomycin A1 (BafA1), an inhibitor of V-
169 ATPases prevents luminal acidification²⁴. Notably, dissipation of the luminal pH with BafA1
170 and the lysosomotropic agent NH₄Cl gave rise to intracellular 5B2-positive aggregates in
171 prion-infected cells (Fig. 2F), suggesting that truncation of nascent full-length (FL)-PrP^d is
172 blocked upon inhibition of pH-dependent proteinases, thus excluding crypticity as cause for
173 the failure to detect intracellular FL-PrP^d. Data on cryptic epitopes and the putative β-
174 cleavage site of PrP are summarised in Fig. 2G.

175 In summary, we provide evidence that nascent PrP^d undergoes proteolytic processing in a
176 pH-sensitive manner, while core mAbs fail to detect abnormal PrP under native conditions
177 due to crypticity of their corresponding binding sites. In contrast, elongating PrP^d fibrils at the
178 plasma membrane can be labelled with N-terminal mAbs under native conditions in
179 agreement with Rouvinski et al.¹⁴. These results suggest existence of two distinct
180 aggregated PrP^d species in prion-infected cells, nascent FL-PrP^d which is associated with
181 fibril elongation at the plasma membrane and a truncated (TR-) PrP^d type at perinuclear
182 sites. Evidence that these two PrP^d types are conformationally distinct at the level of the
183 octapeptide repeat region (OPR) is suggested by the binding propensities of the
184 monospecific anti-PrP mAb Saf32 which labels FL-PrP^d at the plasma membrane under
185 native conditions, but TR-PrP^d at perinuclear sites under denaturing conditions.

186 **Formation of PrP^d fibrils at the plasma membrane is associated with synaptic vesicle** 187 **trafficking and sensitive to cholesterol-lowering.**

188 We next examined whether the antibody pair 5B2/6D11 may provide further insight into the
189 mode of fibril formation at the plasma membrane. At subdiffraction resolution, 6D11-positive
190 puncta can be detected at close proximity to 5B2-positive fibrils, suggesting that TR-PrP^d
191 aggregates are recruited to membrane areas where PrP^d fibril form (Fig. 3A). A pivotal
192 question is thus whether TR-PrP^d reaches the plasma membrane by passive diffusion or by
193 vesicular transport. Triple labelling of prion-infected cells with Synapsin 1 (Syn1), a marker
194 for synaptic vesicles and anti-PrP mAbs 6D11/5B2 provides first evidence that PrP^d may
195 reach the plasma membrane by vesicular transport (Fig. 3B). Single-, double- and triple-
196 labelled puncta can be detected at focal planes above the nucleus and underscore the
197 heterogeneity of overlapping distribution patterns. Double-labelling of PrP^d and integrin β1, a
198 membrane spanning protein which favourably visualises plasma membrane boundaries
199 demonstrates that PrP^d is detected proximal to (short hatched arrows) and at the level of
200 (long straight arrows) the plasma membrane (Fig. 3C), suggesting that PrP^d may dock and
201 fuse with the plasma membrane.

202 Since lowering cholesterol impairs the docking and fusion of transport vesicles with the
203 plasma membrane^{25, 26}, we incubated cells with the cholesterol-lowering agent methyl-β
204 cyclodextrin (mβCD) in a dose-dependent manner to reduce cellular cholesterol. While
205 cellular cholesterol levels decreased by 30-40% under these conditions, cytotoxic effects,
206 measured by a sensitive ATP assay, were absent below 1 mM mβCD (Fig. 3D). Notably, at
207 0.4 mM mβCD, the fluorescence intensities of 6D11 and 5B2 decreased considerably at the
208 plasma membrane, while 6D11-positive PrP^d aggregates were still detected intracellularly at
209 perinuclear sites (Fig. 3E). Quantitative analysis of fluorescence areas confirmed a

210 significant reduction of 5B2 fluorescence and 6D11/5B2 colocalisation, respectively, at a
211 concentration range between 0.4 mM and 0.8 mM m β CD (Fig. 3F). In summary, the lowering
212 of cellular cholesterol levels suggests (i) that intra- and extracellular pools of PrP^d can be
213 uncoupled and (ii) that blocking of PrP^d transport to the plasma membrane inhibits the
214 formation of FL-PrP^d at the plasma membrane.

215 **PrP^d is segregated into vesicles of the regulated secretory pathway and colocalises** 216 **with markers of the endosomal pathway**

217 Experimental evidence that PrP^d colocalises with a marker for synaptic vesicles (Fig. 3B)
218 prompted us to further investigate the contribution of other secretory pathways to PrP^d
219 trafficking. Perinuclear PrP^d colocalises with protein markers of large dense-core
220 (Secretogranin 2 (Scg2)), synaptic (Syn1) and immature (Vesicle-associated membrane
221 protein 4 (Vamp4)) vesicles (Fig. 4 A-C), providing evidence that PrP^d egresses cells by
222 regulated exocytosis. In contrast, no colocalisation between PrP^d and Collagen 4 (Col4), an
223 extracellular matrix protein that is constitutively secreted, was observed (Fig. 4D).
224 Colocalisation of PrP^d with Syn1 is frequently observed at cell junctions as evident by SIM
225 (Fig. 4E). Notably, at the ECM, 5B2-positive FL-PrP^d fibrils are decorated with Syn1 (Fig.
226 4F). To map the route of PrP^d aggregates from perinuclear sites to the plasma membrane,
227 we determined the degree of 6D11 colocalisation, expressed as Pearson correlation
228 coefficient, with markers of the ER (P4hb), Golgi network (β -Cop, Grasp55, Gm130),
229 secretory vesicles (Syp, Vamp4, Syn1, Scg2, Chga, Col4) and endosomal/lysosomal
230 markers (Eea1, Lamp1) (Fig. 4G, H). Representative images for all studied marker proteins,
231 co-labelled with 6D11 can be found in Fig. S5. This result confirms a role of the vesicular
232 secretory pathways and the endosomal/lysosomal system in PrP^d trafficking.

233 **PrP^d internalisation is dependent on functional dynamin and Cdc42**

234 We next investigated whether perturbation of endocytosis affects the prion steady state level
235 of persistently infected cells. While evidence suggests that PrP^c is internalised via clathrin-
236 dependent endocytosis, mediated by its N-terminal domain^{27, 28}, the mode of PrP^d
237 endocytosis remains obscure. We here targeted known regulators of clathrin-dependent
238 endocytosis (CME) and clathrin-independent endocytosis (CIE) pathways, using
239 pharmacological inhibitors and RNA interference.

240 Absence of toxicity was carefully monitored for all inhibitor studies and toxic thresholds are
241 reported in Table S3. Two pharmacological dynamin inhibitors, dynasore²⁹ and dynole³⁰
242 showed a strong dose-dependent decrease of cellular prion steady state levels by as much
243 as 90% over three days (Fig. 5A). However, the clathrin inhibitor Pitstop 2³¹ did not affect
244 prion steady state levels. Further, the macropinocytosis inhibitor Amiloride³² and the actin
245 polymerisation inhibitor Cytochalasin D showed moderate effects on prion steady state
246 levels (Fig. 5A). Two frequently used inhibitors, the CIE inhibitor EGA and Vacuolin which
247 induces vacuole formation by homotypic fusion of endosomes and lysosomes³³, reduced
248 prion steady state levels significantly by 60% and 80%, respectively (Table S4), but the
249 molecular targets of either inhibitor remains unknown.

250 To corroborate a role of CIE pathways in the maintenance of cellular prion steady state
251 levels, we next targeted key regulators of endocytic pathways using RNA interference. To
252 effectively silence gene expression, we used pools of 30 custom-designed siRNAs (siPools)
253 (Hannus et al., 2014) per gene target. We first tested the use of siPools by silencing *Prnp*,
254 since a loss of *Prnp* expression directly compromises prion propagation. Knockdown of *Prnp*
255 leads to a 86% decrease in *Prnp* expression levels, measured by qPCR, when compared to
256 a non-targeting control (NT control, Fig. 5B). To verify that transient *Prnp* knockdown

257 persists over 3 days of culture, we next examined the time-dependence of gene knockdown,
258 following conventional versus reverse transfection of cells. Reverse transfection, where
259 siPools are directly mixed with suspended cells leads to a fast and sustained knockdown of
260 *Prnp* levels over the duration of 72 hours, while conventional transfection, where siPools are
261 added to adherent cells 16 hrs after plating leads to higher variance and lower knockdown
262 efficacies (Fig. 5C). That RNA silencing of *Prnp* by reverse transfection leads to efficient
263 curing of prion-infected cells is corroborated by labelling cells with discriminatory anti-PrP
264 mAbs (Fig. 5D). Following proof of concept for the use of siPools in modulating prion steady-
265 state levels, we next targeted key regulatory genes involved in endocytosis. Levels of
266 knockdown for individual gene targets are reported in Table S5. Despite a 98% knockdown
267 of gene expression, clathrin a (*Clta*) loss-of-function did not affect prion steady state levels
268 (Fig. 5E). Knockdown of the dynamin isoforms *Dnm1* and *Dnm2* led to a decrease of prion
269 steady state levels by 20-30% in single knockdown experiments, while double-knockdown
270 resulted in a 50% decrease in prion steady state levels (Fig. 5E). A highly efficient
271 knockdown of cell division cycle 42 (*Cdc42*) by 97% led to a 50% drop of cellular prion titres,
272 suggested that *Cdc42*-mediated CIE plays an important role in maintaining prion steady
273 state levels. Conversely, depletion of ADP ribosylation factor 6 (*Arf6*), Ras homolog family
274 member A (*Rhoa*), *Arf1* and Caveolin 1 (*Cav1*) did not affect prion steady state levels (Fig.
275 5E). In summary, we provide evidence that prion propagation in *N2a* cells is dependent on
276 functional dynamin and *Cdc42*, but independent of clathrin.

277 **Evaluating the minimum contact time required for productive infection**

278 Due to the lack of PrP^d-specific anti-PrP mAbs, the kinetics of *de novo* PrP conversion is one
279 of the most unexplored questions. While Goold et al., who expressed myc-tagged PrP to
280 distinguish between PrP^c and PrP^{Sc} suggested that *de novo* conversion commences within
281 minutes after infection¹³, Yamasaki et al., who used a PrP^{Sc}-preferring mAb suggested that
282 PrP^{Sc} is formed within days after infection³⁴.

283 To investigate discordances in the kinetics of PrP^d formation, we first determined the
284 minimum contact time for prions with cells required for productive infection to occur,
285 henceforth termed “contact time”. Productive infection is here defined as an infectious event
286 that leads to persistent prion infection. We thus monitored incremental changes of the cell
287 infectious state over several passages after infection in relation to the initial contact time
288 using the Scrapie cell assay (SCA). As depicted in the schematic of Fig. 5F, we infected S7
289 cells with the mouse-adapted prion strain RML on a time-scale between 2 minutes and 24
290 hours in parallel, followed by gentle washing of cells to remove the inoculum. Cells were
291 then grown to confluence and passaged three times before the proportion of infected cells in
292 the total cell population was determined. The relationship between contact time and the
293 percentage of infected cells, following two weeks of cell culture is depicted in Fig. 5G and the
294 corresponding mean percent infection rates were included in the lower panel of Fig. 5F. This
295 confirms that a contact time of 2 minutes suffices to infect neuronal cells, while the mean
296 contact time required for infecting 50% of the cell population, defined as PI₅₀ (PI for
297 productive infection) is 4 hours. Furthermore, a 2- to 4-fold increase in the percentage of
298 infected cells between subsequent cell passages confirms stable propagation of prions (Fig.
299 5H). When plotted as a linear-log graph, a highly correlated linear relationship between the
300 logarithm of contact time and the percentage of infected cells is apparent from 30 minutes to
301 24 hours, while a minor cell population undergoing fast infection after 2 minutes of contact
302 time is the non-linear region of the plot (Fig. 5I).

303 We next addressed the problem of residual inoculum. Crude brain homogenates from mice
304 at disease end stage, typically used for infections, are a non-physiological source of

305 infectivity and may present unspecific effects. We thus tested alternative prion sources.
306 Exosomes are biological nanoparticles that are formed from late endosomes by inward
307 budding into multivesicular bodies^{35, 36} and are constitutively shed into the cell supernatant
308 by prion-infected cells³⁷. When compared to RML, infectious exosomes showed a 10-fold
309 lower immuno-positive background (residual inoculum) following infection (Fig. S6A) and
310 lower toxicity at high infectious doses (Fig. S6B). Following infection of replication-
311 incompetent *Prnp*^{-/-} cells with exosomes from chronically infected iS7 cells, 6D11-positive
312 spots were detected intracellularly 1, 2 and 3 days after infection (Fig. S6A). Remarkably,
313 5B2-positive FL-PrP^d was not detected in susceptible S7 cells prior to 2 day after infection
314 (Fig. 5J and Fig. S6C), indicating that the formation of fibril-like PrP^d at the plasma
315 membrane significantly lags behind infection.

316 **Prion infection leads to PrP conversion at two distinct cellular locations and precedes** 317 **the formation of FL-PrP^d**

318 While a contact time of 2 minutes suffices to infect neuronal cells (Fig. 5F-I), early events
319 after prion infection cannot be resolved using anti-PrP mAbs. We therefore generated a cell
320 model expressing myc-tagged versions of PrP to distinguish newly formed abnormal PrP
321 from inoculum. Myc-tagged *Prnp* chimera were expressed in PK1 cells where endogenous
322 *Prnp* is stably silenced with a small hairpin RNA targeting the 3'-UTR of *Prnp*¹³. Our data on
323 truncation and crypticity of PrP epitopes (Fig. 2D-G) provides guiding information for a
324 rational design of N-terminally tagged PrP variants and suggests that the OPR meets critical
325 prerequisites for monitoring *de novo* PrP conversion. To test this hypothesis, we generated
326 the myc-PrP fusion proteins Gly30-myc PrP (henceforth G30 PrP), G45 PrP, G70 PrP (OPR)
327 and Q90 PrP (CC2) as depicted in Fig. 6A and characterised the tagged fusion proteins.
328 Susceptibility to prion infection of myc-*Prnp* expressing cells, inferred from the number of
329 PrP^{Sc}-positive cells following infection with RML prions, increased in the order G30 PrP, G45
330 PrP to G70 PrP, while Q90 PrP was refractory to infection (Fig. 6B). Notably, failure in
331 detecting intracellular myc-tagged PrP^d in persistently infected G30 and G45, but not in G70
332 PrP-expressing cells under denaturing conditions confirms that PrP^d is N-terminally
333 truncated at a site prior to G70 (Fig. S6C). Remarkably, the myc tag is rendered cryptic in
334 G70 PrP^d which can be unambiguously shown in persistently infected G70 PrP-expressing
335 cells treated in absence and presence of GTC (Fig. S6D). While myc-tagged PrP^d can be
336 distinguished from PrP^c in uninfected cells by fluorescence intensity and the granularity of
337 PrP^d aggregates, respectively (Fig. S6C), we colabelled cells with the discriminatory anti-PrP
338 mAb 6D11 and anti-myc to unambiguously detect infected cells (Fig. 6C-F).

339 Next, we interrogated *de novo* PrP conversion in G70 *Prnp*-expressing cells, infected with
340 RML or exosomes, according to the experimental design in Fig. 5F. Notably, infection of
341 cells with exosomes gave rise to myc-tagged PrP^d in two distinct subcellular sites, the
342 plasma membrane and perinuclear sites as early as 2 minutes after infection (Fig. 6C). We
343 next identified the sites of PrP conversion at 2 and 15 minutes after infection. Irrespective of
344 the source of inoculum, myc PrP^d aggregates were detected in perinuclear regions (Peri), at
345 the plasma membrane (PM) or in either location as depicted by Venn diagrams in Fig. 6D.
346 All experiments were scored independently by three investigators and data is summarised in
347 Table S6. This suggests that abnormal PrP is formed rapidly after infection at two distinct
348 cellular locations, the plasma membrane and an unidentified location at perinuclear sites of
349 neuronal cells.

350 We next determined the proportion of phenotypic cells at early time points after infection with
351 RML prions (Fig. 6E). Cells bearing *de novo* converted PrP (6D11/myc double-labelled) or
352 6D11-positive PrP (abnormal PrP or inoculum) account for less than 1% of the total cell

353 population at 2 and 15 minutes and 3.3 % at 4 hours after infection. For comparison, we
354 reblotted the number of prion-infected cells following 2 weeks of tissue culture, representing
355 perpetuating prion propagation after infection (Fig. 5G). An up to 80-fold increase in the
356 number of prion-infected cells at 2 weeks, compared to the initial myc PrP^d-bearing cells
357 suggests that a unexpectedly low number of cells becomes infected initially, while prion
358 replication and cell-to-cell transmission account for the rapid spread of prions.

359 To address the discrepancy between the fast kinetics of PrP conversion and the delayed
360 formation of FL-PrP^d, we infected G70 PrP-expressing cells according to Fig. 6E and
361 labelled them with the discriminatory anti-PrP mAb pair 5B2/6D11 (Fig. 6F). Notably, 5B2-
362 positive cells could not be detected before 24 hours after infection, suggesting that *de novo*
363 PrP conversion precedes nascent FL-PrP^d fibril formation at the plasma membrane.

364 **Discussion**

365 The self-perpetuating replication of prions is a central tenet of prion pathogenesis and
366 represents a prototypic non-nucleic acid based mechanism of infection and heritability. While
367 long believed to be unique to prions, self-assembly and aggregation of proteopathic seeds is
368 now considered a common trait of amyloids in many neurodegenerative diseases, including
369 Alzheimer's and Parkinson's disease. It is therefore pivotal to identify common and specific
370 disease pathways to assess potential risk and therapeutic strategies alike. This study has
371 advanced our knowledge on the molecular underpinning of prion propagation in several
372 ways.

373 **Elongation of fibril-like PrP^d aggregates, directional transport of prion seeds and fibril** 374 **fragmentation**

375 Built on our initial observation of distinct PrP^d phenotypes in neuronal cells and primary
376 astrocytes, we provide evidence that extracellular fibril-like FL-PrP^d is exclusively formed
377 and elongated at the plasma membrane. In contrast, proteolytically truncated TR-PrP^d
378 aggregates reside at perinuclear sites and segregate into the regulated exocytotic pathway,
379 where they dock and fuse with the plasma membrane, thus providing evidence for a
380 directional transport of PrP^d seeds, opposed to passive diffusion. We further provide
381 evidence that FL-PrP^d gives rise to distinct aggregation states, where the charge cluster 2
382 region remains cryptic under denaturing conditions over extended segments, suggesting that
383 amorphous and fibrillar aggregates may co-exist during fibril formation at the plasma
384 membrane. Notably, N-terminally truncated TR-PrP^d at perinuclear sites fails to form
385 amyloidogenic aggregates which suggests that the PrP N-terminus might be necessary for
386 fibril formation. This is in agreement with the notion that the N-terminus mediates higher-
387 order aggregation processes³⁸⁻⁴⁰. Owing to the lack of amyloidogenic properties, TR-PrP^d
388 may represent amorphous aggregates or oligomers.

389 That the prion state of cells is dependent on functional dynamins and Cdc42 implies that
390 reuptake of PrP^d aggregates in prion-infected cells is critical to maintain prion propagation.
391 While PrP^c is believed to be internalised via CME²⁸, we provide evidence that PrP^d reuptake
392 is mediated by CIE. This notion is associated with another important aspect of PrP^d turnover,
393 proteolytic processing. In keeping with the observation that FL-PrP^d is absent intracellularly,
394 unless cells are treated with BafA1, proteolytic processing of FL-PrP^d following reuptake
395 provides a chaperon-independent cellular mechanism for fibril fragmentation, a cellular
396 process that is considered critical to maintain prion replication. In contrast, prion propagation
397 in yeast is believed to be strongly dependent on chaperon activity^{41, 42}.

398 **Kinetics of PrP conversion and nascent FL-PrP^d formation**

399 We provide evidence that PrP conversion occurs within minutes after infection at two distinct
400 cellular locations, the plasma membrane and an unidentified perinuclear site. This result
401 accommodates opposing views on the primary sites of PrP conversion^{6, 9, 13}, but also
402 supports the notion of a fast rate of PrP conversion¹³. We think that labelling of cells under
403 non-denaturing condition may explain why intracellular PrP conversion was not observed in
404 the Goold study¹³. Our study provides two further important aspects of seeded PrP^d
405 aggregation.

406 Firstly, despite the fast rate of PrP conversion, formation of FL-PrP^d aggregates was not
407 detected prior to 24 hours after infection. This suggests (i) that the formation of truncated
408 PrP species is energetically favoured and (ii) that the infectious seeds that trigger the fast
409 formation of TR-myc PrP^d at both cellular conversion sites are N-terminally truncated.
410 Notably, non-fibrillar amorphous oligomers are thought to represent the most infectious
411 seeds for prion propagation^{43, 44}, although their state of proteolytic processing remains
412 unknown. While the presence of truncated versions of PrP^{Sc} and PrP^c in prion diseases has
413 been widely reported⁴⁵⁻⁴⁹, this study provides new insight into the formation and the
414 molecular relationship between truncated and full-length versions of PrP^d. In extension to
415 current models of PrP^d formation (for review see⁵⁰), we propose that the conformational
416 transition from PrP seeds to fibrils is favoured by neutral pH conditions and can be blocked
417 by retaining PrP^d seeds at an acidic luminal pH.

418 Secondly, the frequency of *de novo* PrP conversion is much lower than previously
419 suggested¹³, as verified by correlative imaging and prion titre output methods for various
420 contact times. While *de novo* conversion was observed at a frequency of only 0.1%, 0.2%
421 and 0.6% for a contact time of 2 min, 15 min and 4 hours, respectively, prion titres increased
422 up to 80-fold when cells were serially passaged for 2 weeks. This suggests that cell-to-cell
423 transmission is a crucial cellular mechanism that underpins prion propagation.

424 We provide evidence that PrP^d segregates into synaptic and large-dense core vesicles of the
425 regulated exocytosis pathway. Notably, peptide hormones and neuropeptides are thought to
426 be sorted into immature secretory granules by virtue of protein aggregation⁵¹⁻⁵⁴, suggesting
427 that prions may be sorted into the secretory pathway by default. Importantly, the self-
428 assembly of functional amyloids is reversible and more information on the reversibility of the
429 amyloid-like aggregation state of peptide hormones and neuropeptides⁵² will be critical to
430 understand proteopathic seeds. Our finding that PrP^d aggregates are detected in synaptic
431 vesicles may further provide an important link between prion propagation and pathogenesis,
432 since synaptic dysfunction is considered an early pathogenic process in
433 neurodegeneration⁵⁵.

434

435 **Methods**

436 **Antibodies and reagents**

437 The antibodies used in this study were summarised as follows (clone, company, catalogue number):
438 Mouse monoclonal anti-PrP (8H4, Sigma, P0110), rat monoclonal Lamp1 (1D4B, Santa Cruz
439 Biotechnology (SCB), sc-19992), mouse monoclonal anti-PrP (5B2, SCB, sc-47730), mouse
440 monoclonal anti-PrP (AH6, SCB, sc-69896), mouse monoclonal anti-PrP (8B4, SCB, sc-47729),
441 mouse monoclonal anti-Syp (7.2, Synaptic Systems, 101 011), rabbit polyclonal anti-Vamp4 (Synaptic
442 Systems, 136 002), rabbit polyclonal anti-Chga (Synaptic Systems, 259 003), rabbit polyclonal anti-
443 phospho FAK (pY397, Thermo Fisher Scientific, 44-624G), rabbit polyclonal anti-beta Cop (Thermo
444 Fisher Scientific, PA1-061), rabbit polyclonal anti-Scg2 (Abcam, ab12241), mouse monoclonal anti-
445 PrP (7D9, Abcam, ab14219), rabbit polyclonal anti Col4 (AbD Serotech, 2150-1470), rat monoclonal
446 anti-CD29 (9EG7, BD Biosciences, 553715), mouse monoclonal anti-GM130 (35, BD Biosciences,

447 610822), mouse monoclonal anti-PrP (6D11, BioLegend, 808002), mouse monoclonal anti-PrP
448 (Saf32, Cayman, 189720), rabbit monoclonal anti-PDI (C81H6, Cell Signaling Technology, 3501S),
449 rabbit monoclonal anti-Eea1 (C45B10, Cell Signaling Technology, 3288), rabbit polyclonal anti-Lc3a
450 (Cell Signaling Technology, 4599), rabbit polyclonal anti-GFAP (DAKO, Z0334), Mouse monoclonal
451 anti-PrP (3F4, Merck, MAB1562), mouse monoclonal anti-PrP (MAB5424, Merck, MAB5424), mouse
452 monoclonal anti-myc, AF 488-conjugated (9E10, Merck, 16-308), rabbit polyclonal anti-Syp1
453 (Millipore, AB1543), mouse monoclonal anti-Snap25 (SP14, Millipore, MAB331), rabbit polyclonal
454 anti-Gorasp2 (Grasp55) (Proteintech, 10598-1-AP), mouse monoclonal anti-PrP (AG4, TSE
455 Resources Centre, TSE RC, RC 059), mouse monoclonal anti-PrP (GE8, TSE Resources Centre,
456 TSE RC, RC 061), ICSM18 (UCL Institute of Prion Diseases). The reagents in this study were
457 summarised as follows (company, catalogue number): Dynasore (Cambridge Bioscience, 1900-25),
458 Pitstop 2 (Generon, AOB3600-25), Bafilomycin A1 (Insight Biotechnology, BIV-1829-250), Dynole
459 (Insight Biotechnology, sc-362731), Cytochalasin D (Cambridge Bioscience, B1176-5), Cell Titre Glo
460 luminescent cell viability assay (Promega, G7571), Lipofectamine RNAimax transfection reagent
461 (Thermo Fisher Scientific, 13778150), Pierce LDH cytotoxicity assay (Thermo Fisher Scientific,
462 C20301), Amplex Red assay (Thermo Fisher Scientific, A12216), One Shot TOP10 chemically
463 competent E.Coli (Thermo Fisher Scientific, C404010).

464 **Cell Lines and Tissue Culture**

465 Prion-infected and uninfected mouse neuroblastoma N2a-derived cell lines were maintained in
466 OptiMEM, containing 10% foetal calf serum (FBS) and 1% penicillin/streptomycin (OFCS). The highly
467 prion-susceptible cell line S7 was derived from N2aPK1 cells as previously reported in Marbiah et al.⁵⁶
468 and was split twice weekly for cell maintenance. Where S7 cells were grown for extended culture
469 times (Fig. 1C), the serum concentration was reduced by 50 %, while the culture medium was
470 changed daily from 3 days of culture. Under these conditions, the build-up of rod-like PrP^d aggregates
471 at the plasma membrane is observed from three days onwards. Daily replacement of ½ the
472 conditioned medium with fresh OFCS from 3 days of culture was alternatively used for extended
473 tissue culture times where specified.

474 **Primary neuronal cultures**

475 Primary cortico-hippocampal cultures were prepared from embryonic e17 FVB mouse brains
476 essentially as described previously⁵⁷. Primary neuronal cultures were maintained in Neurobasal
477 medium, supplemented with 2% (v/v) B27, 0.25% (v/v) GlutaMAX and 1% penicillin/streptomycin
478 (Pen/Strep). Where primary neuronal cultures were maintained up to four weeks, half the medium
479 was replaced with fresh medium twice a week. All mouse experiments were performed under
480 approval and license granted by the UK Home Office (Animals (Scientific Procedures) Act 1986),
481 project license number 70/9022 in compliance with UCL institutional guidelines and Animal Research:
482 Reporting of In Vivo Experiments (ARRIVE) guidelines (www.nc3rs.org.uk/ARRIVE/).

483 **Prion infection of cultured cells**

484 To infect prion-permissive cells, aliquots of 5×10^4 S7 cells/ml OFCS were plated into wells of 96-well
485 plates. Sixteen hours later, cells were infected with serially 1:10 diluted ribolysed RML brain
486 homogenates. Cells were typically infected with 10^{-4} or serial 1:10 dilutions of 10% brain
487 homogenates (w/v) from prion-diseased mice at clinical disease with a titre of $10^{8.4}$ LD50 units/g.
488 Following infection, cells were grown to confluence and split three times 1:8 to dilute out PrP^{Sc}-
489 positive inoculum. At each split after reaching confluence, the proportion of PrP^{Sc}-positive cells was
490 determined by the Scrapie cell assay (SCA) as specified in "Quantification of prion infection rates".

491 **Minimum contact time for productive infection**

492 To determine the minimum contact time for productive infection (Fig. 5 F-I), prion-susceptible S7 cells
493 were infected with clarified RML brain homogenates to reduce the amount of residual immune-
494 positive inoculum, detected as background in the Scrapie cell assay (SCA) and diluted out by serial
495 cell passages⁵⁸. RML brain homogenates were clarified by centrifugation at $300 \times g$ for 10 min. To
496 monitor the amount of residual inoculum in clarified RML homogenates, prion replication-refractory
497 *Prnp*^{-/-} cells (see "Generation of Prnp knockout cells using Crispr-Cas9" below) were plated out in

498 parallel experiments and infected with clarified RML brain homogenate alongside with S7 cells.
499 Residual inoculum, detected in Prnp^{-/-} cells was less than 10% of the total signal in prion-susceptible
500 cells after the first passage and less than 1% after the second passage, confirming that residual
501 inoculum in clarified RML homogenates is rapidly diluted out during sequential passaging of cells. To
502 assess the minimum contact time for productive infection, aliquots of 5 x 10⁴ S7 cells/ml OFCS were
503 plated into wells of 96-well plates and infected with a 1 x 10⁻⁴ dilution of clarified RML brain
504 homogenate the following day. After varying time points after infection, ranging from 2 min to 24 h
505 (Fig. 5F), cells were carefully washed with PBS to remove the inoculum, grown to confluency and the
506 number of infected cells was determined in subsequent cell passaged (Fig. 5 G-H).

507 **Quantification of prion infection rates**

508 The number of prion-infected cells following infection with prion-containing media was determined
509 using the Scrapie Cell Assay (SCA) as described previously⁵⁸. The SCA is based on the microscopic
510 detection of proteinase K-resistant PrP (PrP^{Sc}) in prion-permissive cells in an automated manner
511 using a Biomek FX liquid handling robot. Suspended cells (approximately 25,000 cells) were
512 transferred onto ELISPOT (Multi Screen Immobilon-P, Millipore, UK) plates. ELISPOT plates were
513 vacuum-drained and dried at 50°C prior to storage at 4°C until further processing. Where prion titres
514 in persistently infected cells were determined, suspended cells were diluted in PBS 1:10 and
515 approximately 2,000 cells per well were transferred onto ELISPOT plates. The number of cells was
516 determined by Trypan blue as specified below. The revelation and quantification of PrP^{Sc}-positive
517 cells was done essentially as described in Schmidt et al.⁵⁹ using a Bioreader 5000-EB system
518 (BioSys, Karben, Germany). Changes in the prion steady state levels of persistently infected cells
519 following incubation with small inhibitory molecules or siRNA were also quantified by SCA. Where the
520 percentage of infected cells on a population level was quantified in subsequent passages (Fig. 5 G-I),
521 the total number of cells was determined in parallel experiments by transferring approximately 1,000
522 cells per ml onto ELISPOT plates. Subsequently, plates were stained with Trypan blue in cell lysis
523 buffer (50 mM Tris HCl, 150 mM NaCl, 0.5% (w/v) sodium deoxycholate and 0.5% (v/v) Triton-X 100,
524 pH 8.0) and counted with the Bioreader 5000-EB to determine the total number of transferred cells.

525 We further used crude exosome fractions as a source of prion infectivity. To isolate exosomes,
526 chronically infected iS7 cells were grown to confluence in 15-cm Petri dishes. After removing the
527 growth medium, cell layers were overlaid with fresh medium and conditioned medium was collected
528 after 24 h for 4 consecutive days. Cell supernatants were stored at 4 °C until further processing.
529 Combined supernatants were cleared from whole cells and cell debris by centrifugations at 300 x g for
530 5 min and at 4,500 x g for 10 min, respectively. Clarified supernatants were then centrifuged at 32,000
531 x rpm for 2 h in a Beckman ultracentrifuge, equipped with SW 32 Ti swinging-bucket rotors (Beckman
532 Coulter UK, High Wycombe, UK). Supernatants were discarded and pellets resuspended in residual
533 medium. Concentrated exosome-containing suspensions were aliquoted and kept at -80C until use.
534 Infectious titres of the exosome concentrates were determined using the SCA, essentially described
535 previously⁵⁸. Typically, one litre of cell supernatant from prion-infected iS7 cells yielded 2-3 millilitres
536 of concentrated exosomal pellet with an infectious titre of 10^{7.88} Tissue culture infectious units
537 (TCIU)/ml.

538 **Cell curing assay**

539 Effects of small molecule inhibitors on the prion steady state levels were determined by the SCA while
540 cytotoxicity was carefully monitored. Stock solutions of inhibitors were prepared in DMSO unless
541 specified otherwise in the manufacturer's guidelines. Since 1:1,000 dilutions of DMSO did not affect
542 the cell doubling rates and the prion steady state levels of iS7 cells, the concentration of DMSO-
543 soluble inhibitor stock solutions was adjusted to allow dilutions of at least 1:1,000 or higher. To
544 determine effects of small molecule inhibitors on prion steady state levels, 300 µl aliquots of
545 chronically infected iS7 cells were plated into wells of 96-well plates at a concentration of 5 x 10⁴ cells
546 per ml OFCS. After 16 hours, cells were incubated with serially diluted inhibitors. After 3 days, cells
547 were resuspended, diluted 1:10 in PBS and 100 µl of the cell suspension was transferred onto
548 ELISPOT plates (Cat#. MSIPN4550, Merck Millipore Ltd, Tullagreen, Ireland) and prion titres were
549 determined. Data in Table S4 represent mean values of at least three independent experiments and
550 are normalised to vehicle (DMSO)-treated cells.

551 **Determination of cell viability and cytotoxic thresholds**

552 Cytotoxicity was assessed by measuring LDH release (Pierce LDH cytotoxicity assay kit, Thermo
553 Fisher Scientific) and ATP levels by Luminescent Cell Viability Assay (Cell Titre Glo, Promega). To
554 take experimental variation into account, cytotoxic effects were scored positive, when a threshold of
555 10% was exceeded, when compared to mock controls. Since cytotoxicity of small molecule inhibitors
556 is highly correlated with the cell density, we determined cytotoxic thresholds of inhibitors for distinct
557 cell densities (see Table S3). In the ATP assay, luminescence values of inhibitor-treated cells were
558 normalised with those of mock-treated cells and changes in ATP levels were recorded. In the LDH
559 assay, the levels of toxicity were calculated as below,

$$\% \text{ cytotoxicity} = \frac{\text{LDH activity (treated)} - \text{LDH activity (unspecific)}}{\text{maximal LDH activity} - \text{LDH activity (unspecific)}} \times 100$$

560 where unspecific LDH activity represents absorbance values of cells treated with 10% water (v/v) and
561 maximal LDH represents absorbance values following cell lysis.

562 To determine the effects of methyl- β -cyclodextrin on cell viability, cholesterol and PrP^d levels,
563 chronically infected iS7 cells were plated into 96-well plates (Cat#: 3505, Scientific Laboratory
564 Supplies Ltd, Nottingham, UK) at a concentration of 5×10^4 cells per ml OFCS. After 16 hours, cells
565 were incubated with methyl- β -cyclodextrin (Cat#: Sc-215379, Santa Cruz Biotechnology, Heidelberg,
566 Germany), dissolved in culture media without FBS, at concentrations specified in Fig. X. To determine
567 the cellular cholesterol levels, cell layers were washed with PBS and lysed in 100 μ l TE buffer (10 mM
568 Tris and 1 mM EDTA, pH 8.0) per well. Aliquots of 50 μ l lysates were transferred into black 96-well
569 microplates (Cat#: 655077, Greiner Bio One Ltd, Gloucestershire, UK) and cholesterol levels were
570 determined using the Amplex red assay (Cat#: A12216, Thermo Fisher Scientific, Loughborough, UK)
571 according to the manufacturer's specification. Cell viabilities were analysed by CellTiter-Glo
572 luminescent cell viability assay (Cat#: G7571, Promega, Southampton, UK).

573 **Processing of cells for imaging**

574 For immunolabelling, cells were processed as specified previously⁵⁶. Briefly, cells were fixed with 3.7
575 % formalin (Thermo Fisher Scientific, Loughborough, UK) in PBS for 12 min. Unless otherwise
576 specified, cells were washed with chilled acetone for 1 min. After rehydration with PBS, cells were
577 incubated with 3.5M guanidine thiocyanate (GTC, Melford) for 10 min. Cells were washed at least five
578 times with PBS prior to labelling with primary antibodies, diluted into Superblock (Thermo Fisher
579 Scientific)/PBS (1:4), supplemented with 10% Pen/Strep and incubated at 4° C overnight. After
580 washing with PBS, cells were labelled with highly cross-adsorbed fluorescence-conjugated secondary
581 antibodies (AffiniPure, Jackson ImmunoResearch) and incubated at 4° C overnight. Cells were
582 imaged after a final wash with PBS.

583 **Image acquisition using laser-scanning microscopy**

584 Images were acquired with a Zeiss LSM710 laser-scanning microscope, equipped with a 63 x
585 objective (1.4 oil, Plan-Apochromat) using immersion oil Immersol 518F (Carl Zeiss, Cambridge, UK).
586 Cells were fixed and treated as described above. Cells were labelled with fluorescence-conjugated
587 secondary antibodies (AffiniPure, Jackson ImmunoResearch) and Alexa Fluor 488 and Rhodamine
588 Red-X fluorescence was measured using a 460-540 nm and 565-640 nm bandpass filters,
589 respectively, following excitation with an argon laser at 488 nm and a diode-pumped solid state laser
590 at 561 nm, respectively. To unambiguously distinguish PrP^d deposits at distinct cellular sites, i.e. the
591 plasma membrane, perinuclear regions and the extracellular matrix (ECM), we conducted serial z-
592 stacks and normalised the focal planes using ECM-resident focal adhesion kinase (FAK). Notably, in-
593 focus detection of FAK, labelled with an anti-FAK antibody coincides with in-focus detection of PrP
594 and was arbitrarily denoted "zero μ m" as a focal reference level with an estimated standard deviation
595 of $\pm 0.2 \mu$ m.

596 **Structural Illumination Microscopy**

597 To image PrP^d rods at the plasma membrane and ECM, cells were grown for extended culture times
598 (5-7 days) with daily medium changes from day 4. Cells were processed as specified in “Processing
599 of cells for imaging” and labelled with anti-PrP antibodies 5B2 and 6D11, followed by highly cross-
600 adsorbed secondary antibodies, anti-mouse IgG1-Rhodamine and anti-mouse IgG2a-Alexa Fluor 488
601 (AffiniPure, Jackson ImmunoResearch), respectively. Images were acquired by Structured
602 Illumination Microscopy (SIM) using a Zeiss ELYRA PS.1 microscope with Plan-Apochromat DIC M27
603 63X objective and 1.4 immersion oil. Images were acquired using 5 phase shifts and 3 grid rotations
604 for the 561 nm and 488 nm lasers at a 5-10% output. Images were acquired using a sCMOS
605 (pco.edge sCMOS) camera. Channels were aligned using a slide with multi-coloured beads (100 nm,
606 TetraSpeck microspheres T7279, Thermo Fisher Scientific) with the same image acquisition settings.
607 After SIM reconstruction and channel alignment, images were concatenated into a single image stack.
608 Images were processed with ZEN black version 11.0.2 software (Zeiss).

609 **Quantifying relative PrP^d fluorescence intensities**

610 Chronically prion-infected and uninfected cells were seeded into 8-well chamber slides and grown to
611 confluence prior to processing as described in “Processing of cells for imaging”. Quantitative analysis
612 of PrP^d aggregates at perinuclear and extracellular sites was conducted following double-labelling of
613 cells with anti-PrP antibodies 5B2 and 6D11 overnight at 4°C. After washing with PBS, cells were
614 labelled with highly cross-adsorbed isotype-specific fluorescence-conjugated secondary antibodies
615 (AffiniPure, Jackson ImmunoResearch) for 12-24h. Randomly selected fields with 10 to 20 cells were
616 analysed from at least three replicate experiments using Volocity. To quantify fluorescence intensities
617 of PrP^d aggregates, threshold levels of PrP^c fluorescence were determined in uninfected cells and
618 used as baseline levels. To determine levels of colocalisation of 6D11-positive PrP^d with intracellular
619 markers at perinuclear sites, single cells were analysed using the Volocity cropping function. Cells
620 were double-labelled with primaries for 24 hours and washed with PBS. Cells were subsequently
621 labelled with highly cross-adsorbed fluorescence-conjugated secondary antibodies (AffiniPure,
622 Jackson ImmunoResearch) for 24 hours. Levels of colocalisation was determined by Pearson’s
623 correlation with Costes threshold correction⁶⁰ according to the specification of Perkin Elmer, the
624 manufacturer of Volocity.

625 **Validating the specificity of anti-PrP antibodies**

626 To validate the target specificity of anti-PrP antibodies, we generated *Prnp* knockout cells. Briefly, the
627 *Prnp* open reading frame (ORF) in N₂a cells was deleted by CRISPR-Cas9 according to Ran et al.⁶¹.
628 Single guide RNAs (sgRNAs) were selected using the web-based “sgRNA designer” from the Broad
629 Institute and cloned into the Addgene vector pX459 (Ref: 62988) as specified below. Out of four
630 sgRNAs tested for their efficacy of *Prnp* knockdown, sgRNA-*PrnP-69*, which recognises the
631 complementary *Prnp* sequence 53-ATGTCGGCCTCTGCAAAAAG-72 and enables a Cas9-mediated
632 double-strand break at position 69 was found to be superior. To synthesise sgRNA-*PrnP-69*, two
633 oligonucleotides (fw-5'-CACCGATGTCGGCCTCTGCAAAAAG-3' and rev-5'-
634 AAACCTTTTTGCAGAGCCGACATC-3'), flanked by the NGG PAM sequence with overhangs
635 (underlined) were annealed and cloned into the Bpl-digested vector pX459 using T4-polynucleotide
636 kinase ligase (New England Biolabs, Hitchin, UK) according to the specification of the manufacturer.
637 To generate *Prnp* knockout cells, pX459/gRNA-*PrnP-69* was transfected into N2a cells using
638 Lipofectamine LTX/Plus (Thermo Fisher Scientific) as recommended by the manufacturer and cells
639 were selected with 2 µg puromycin per ml of medium.

640 **Cloning of Myc-tagged PrP variants**

641 Double stranded DNA molecules of the full-length mouse *Prnp* gene (Genbank NP_001265185.1)
642 with Myc tag (aa's EQKLISEEDL), inserted at positions p.Gly45, p.Gly70 and p.Glu90 were
643 synthesised by GeneArt (ThermoFisher, UK). Corresponding *Prnp* fragments (10 ng) were Gibson
644 assembled by overlap extension using GeneArt Gibson Assembly HiFi MM (ThermoFisher,
645 Regensburg, Germany) into the linearised pLNXC2 vector (25 ng) (Addgene, Teddington, UK). Vector
646 and inserts at a 1:1 molar ratio were incubated for 1 h on a thermocycler (PCRmax, East Sussex,
647 UK), transformed at 37°C for 1 h in One Shot TOP10 chemically competent E.Coli cells
648 (ThermoFisher, UK) and then plated onto LB agar plates, containing 50 µg/ml ampicillin (Sigma, UK).

649 After overnight culture, positive plasmids were digested with restriction enzymes and analysed by gel
650 electrophoresis to confirm that the insert is in the correct position prior to Sanger sequencing
651 (Eurofins Genomics, Ebersberg, Germany). Mouse *Prnp*, tagged at Gly30 with myc, containing Not1
652 and Xho1 restriction sites was obtained from GeneArt Life Technology. Cloning into the linearised
653 pLNXC2 vector was done as described above. Transformation of competent JS4 cells was carried out
654 in presence of ampicillin overnight. Colonies were screened by PCR to identify those with inserts.
655 Plasmid DNA was extracted and digested and the sequence of Gly30-myc *Prnp* was confirmed by
656 Sanger sequencing.

657 For retroviral production, HEK-293 derivative Phoenix cells were seeded at a concentration of 1×10^6
658 cells per 10 cm plate in producer cell growth media (DMEM, 10 % FCS, 1 % Penicillin-Streptomycin, 1
659 % Glutamine), 24 hrs before transfection with $3 \mu\text{g}$ *Prnp* Myc positive constructs and $12 \mu\text{l}$ Fugene HD
660 (Promega, UK) as per manufacturer's instructions. After 24 h the medium was replaced with fresh
661 growth medium and supernatants were collected at two days after transfection. After filtration of
662 supernatants through $0.45 \mu\text{m}$ filters (Acrodisc Syringe filters, Cat# 4219, PALL Europe, Portsmouth,
663 UK) and supplementation of polybrene ($8 \mu\text{g}/\text{ml}$), PK1-10 Si8 double-knockdown cells¹³ were
664 transduced and incubated at 37°C for 4-5 hrs before replacing with complete media (Optimem, 10 %
665 FCS, 1 % Penicillin-Streptomycin). In the next split the cells were cultured under subsequent selection
666 markers G418 ($200 \mu\text{g}/\text{ml}$, ThermoFisher, UK) and Puromycin ($2 \mu\text{g}/\text{ml}$, Invitrogen, UK) and passaged
667 at least 5 times in presence of antibiotics. A control with empty pLNXC2 vector was set up in parallel
668 experiments to monitor the efficacy of antibiotic selection.

669 **Assessing prion susceptibility of myc-tagged *Prnp***

670 To investigate the permissiveness of myc-*Prnp*-expressing cell lines at position p.Gly30, p.Gly45,
671 p.Gly70 and p.Glu90 to mouse-adapted prion strains, cells were plated out in 96-well culture plates at
672 a concentration of 1×10^5 cells/ml OFCS. The next day, the culture medium was replaced with $300 \mu\text{l}$
673 OFCS, containing 10^{-4} dilutions of RML (10%, w/v) and CD1 (10%, w/v) for mock infections and left
674 until cells were sub-confluent to undergo a split. At passages 3 and 4, respectively, $100 \mu\text{l}$ of a 1:10
675 dilution of cells, resuspended in PBS were transferred onto wells of 96-well Elispot plates
676 (PerkinElmer, UK) to determine the number of PrP^{Sc}-infected cells using Scrapie Cell Assay,
677 essentially as described previously⁵⁸.

678 **Infection and labelling of myc PrP-expressing cells**

679 For immunofluorescence-based detection of myc-tagged PrP^d aggregates, $500 \mu\text{l}$ aliquots of 5×10^4
680 cells per ml OFCS were seeded into 8-well chamber slides (Thermo Scientific, UK). After 16 h, cells
681 were infected with prion-containing media, i.e. RML-prion and uninfected CD1 homogenates or
682 exosome-enriched cell supernatants from persistently infected or uninfected S7 cells. Twenty four hrs
683 following cell plating, the culture medium was replaced with $500 \mu\text{l}$ OFCS, supplemented with a $1 \times$
684 10^{-4} dilution of 10% brain homogenates (RML and CD1 mock) or $30 \mu\text{l}$ exosomes per ml medium. To
685 examine *de novo* PrP conversion following prion infection, myc PrP-expressing cells were grown for 3
686 days prior to infection with brain homogenates or exosome-enriched supernatants as above. Prion-
687 containing solutions were removed by washing with PBS after various time points as specified in Fig.
688 6 and cells were fixed with 4% formalin for 15 min at room temperature. Cells were then incubated
689 with ice cold acetone for 1 min, followed by denaturation with 3.5 M GTC for 10 min at room
690 temperature. The cells were incubated with anti-PrP mAb 6D11 (1:10,000 BioLegend) and directly
691 conjugated mAb AF488 anti-myc 9E10 (1:1,000 Millipore, UK) in Superblock/PBS antibody diluent
692 containing 5% FBS and left overnight at 4°C . AffiniPure Rhodamine Red goat anti-mouse IgG2a
693 subclass secondary antibody was used at a 1:1,000 dilution overnight at 4°C . All images were
694 captured on a Zeiss LSM 700 confocal microscope, equipped with a $63 \times$ oil objective at the same
695 acquisition settings.

696 **Identification of *de novo* PrP conversion sites**

697 To investigate the cellular sites of *de novo* PrP conversion in G70 PrP-expressing cells, threshold
698 levels for the detection of myc-tagged PrP^c were first determined using mock-infected cells and PMT
699 gains were adjusted to exclude background fluorescence. The same settings were then applied to

700 examine the sites of *de novo* PrP conversion in freshly prion-infected cells at the time points specified
701 in Fig. 6C-D. All cells were co-labelled with the discriminatory mAb 6D11 to increase the confidence of
702 scoring *de novo* infected cells. Only double-labelled cells were scored as shown in representative
703 images (Fig. 6C). All experiments were scored independently by three investigators and at least 50
704 myc-PrP^d positive cells were analysed for each condition.

705 **Quantifying infected myc *Prnp* cells**

706 To determine the proportion of infected G70 PrP-expressing cells at early time points after prion
707 infection, three separate automated scans of 9 x 9 tiles with approximately 60 cells per tile were set
708 up for every condition with a 5% overlap among tiles. Background levels were adjusted as specified
709 above. For cell phenotypic analysis, cells double-positive for anti-myc and 6D11 were manually
710 scored based on fluorescence intensity using Zen black 2.3SP1. The total number of cells was
711 determined by scoring DAPI-positive nuclei using Volocity software. To determine the percentage of
712 5B2-positive cells (Fig. 6F), tile scans of 9 x 9 tiles were acquired and cells were scored based on the
713 detection of anti-5B2-positive PrP^d at the plasma membrane.

714 **Transcriptional gene silencing**

715 Transient knockdown of gene expression was conducted by reverse transfection of cells using siRNA
716 pools (siTOOLS Biotech GmbH, Martinsried, Germany) which contain up to 30 siRNAs to achieve
717 maximal transcript coverage and highly efficient gene knockdown. Briefly, siRNA pools were
718 reconstituted with nuclease-free water to a stock concentration of 10 μ M. Two μ l siPool and 6 μ l
719 RNAimax transfection reagent were added to 42 μ l FBS-free OPTIMEM and incubated to form a
720 complex. After 5 min, 950 μ l OFCS were added to the RNA complex and 1 ml of 1.33×10^5 cells
721 (reverse transfection) was added for a final concentration of 6.7×10^5 cells/ml.

722 **Quantifying gene knockdown levels**

723 We used real-time quantitative PCR (RT-qPCR) to determine the level of gene expression in cells,
724 following transcriptional silencing. Briefly, total RNA was isolated 72 hrs after transfection of cells with
725 siPools and a non-targeting control using Direct-zol RNA Mini-prep kit (Cambridge Bioscience,
726 Cambridge, UK). Genomic DNA was removed during RNA isolation as per manufacturer's
727 instructions. RNA purity and concentration was measured spectrophotometrically (Nanodrop 2000,
728 Thermo Scientific, USA). Total RNA (500 ng) was used to synthesise the first strand complementary
729 DNA (cDNA) using QuantiTect Reverse Transcription kit (Qiagen, Manchester, UK). All real-time
730 qPCR reactions were carried out with QuantStudio 12K Flex (Applied Biosystems, Cheshire, UK) with
731 the following cycling parameters: 50°C, 2mins; 94°C, 15min; 40 cycles at 94°C, 15s; 60°C, 1min.
732 Samples were set up in triplicates in 10 μ l reactions containing QuantiTect SYBR Green (Qiagen), 1x
733 QuantiTect customised Primer Assay (lyophilized in TE, pH 8.0), 25ng of cDNA made to a final
734 volume with ddH₂O. Gapdh and Actb were used as endogenous controls for normalising target gene
735 expression levels. Data acquisition of the fluorescent signal was performed at the end of the run to
736 assess the expression of mRNA by evaluating threshold cycle (CT) values. Double delta CT
737 calculations were measured as logarithm and then converted to fold change of 100, after untreated
738 control levels were subtracted from target levels.

739 **Statistics**

740 Data was analysed using SPSS, Graphpad Instat 3.10 and Microsoft Excel. The Kolmogorov-Smirnov
741 test was applied to test whether experimental data were normally distributed. Normally distributed
742 data was analysed by parametric tests, including Student's t-test and Analysis of variance (ANOVA)
743 followed by post-hoc Bonferroni test. In case of small sample sizes (<12) or data that did not fit the
744 normal distribution, Kruskal Wallis and Mann Whitney U test were employed, followed by the Dunn's
745 multiple range test. Unless otherwise stated, a p-value < 0.01 was considered statistically significant.

746

747 **Acknowledgements**

748 This study was funded by the UK Medical Research Council (MRC) and by the UK
749 Biotechnology and Biological Sciences Research Council (BBSRC); S. A. T. was supported
750 by The Francis Crick Institute which receives its core funding from Cancer Research UK
751 (FC001187), the UK Medical Research Council (FC001187). This research was funded in
752 whole, or in part, by the Wellcome Trust (FC001187). For the purpose of Open Access, the
753 author has applied a CC BY public copyright licence to any Author Accepted Manuscript
754 version arising from this submission. We are grateful to Ms Parineeta Arora and Prof Parmjit
755 Jat for providing PK1-10 Si8 double-knockdown cells and a Gly30-myc *Prnp* expression
756 clone. We thank Christian Schmidt, Parvin Ahmed and George Thirlway for technical
757 assistance with Automated Scrapie Cell Assays and the staff of the MRC Prion Unit at UCL
758 Biological Services Facility for animal care and technical assistance. We are grateful to Prof
759 John Collinge for helpful discussion.

760 **Author Contributions**

761 Conceptualization, P.C.K. and S.A.T.; Methodology, J.M.R., M.P., H.H. and P.C.K.;
762 Validation, J.M.R., M.P., H.H. and P.C.K.; Investigation, J.M.R, M.P., H.H. P.C.K;
763 Resources, J.M.R., M.P., P.C.K.; Writing – Original Draft, P.C.K. ; Writing – Review &
764 Editing, S.A.T., J.M.R, M.P. and P.C.K.; Visualization, P.C.K; Project Administration, P.C.K.;
765 Supervision, P.C.K.; Funding Acquisition, P.C.K.

766

767 **Competing Interests**

768 The authors declare no competing interests.

769

770 **References**

- 771 1. Griffith JS. Self Replication and scrapie. *Nature* **215**, 1043-1044 (1967).
772
773 2. Prusiner SB. Scrapie Prions. *Annu Rev Microbiol* **43**, 345-374 (1989).
774
775 3. Prusiner SB. Molecular biology and genetics of prion diseases. *Cold Spring Harbor Symp*
776 *Quant Biol* **61**, 473-493 (1996).
777
778 4. Weissmann C, *et al.* The role of PrP in pathogenesis of experimental scrapie. *Cold Spring*
779 *Harbor Symp Quant Biol* **61**, 511-522 (1996).
780
781 5. Horiuchi M, Karino A, Furuoka H, Ishiguro N, Kimura K, Shinagawa M. Generation of
782 monoclonal antibody that distinguishes PrPSc from PrPC and neutralizes prion infectivity.
783 *Virology* **394**, 200-207 (2009).
784
785 6. Marijanovic Z, Caputo A, Campana V, Zurzolo C. Identification of an Intracellular Site of Prion
786 Conversion. *PLoS Pathog* **5**, (2009).

787

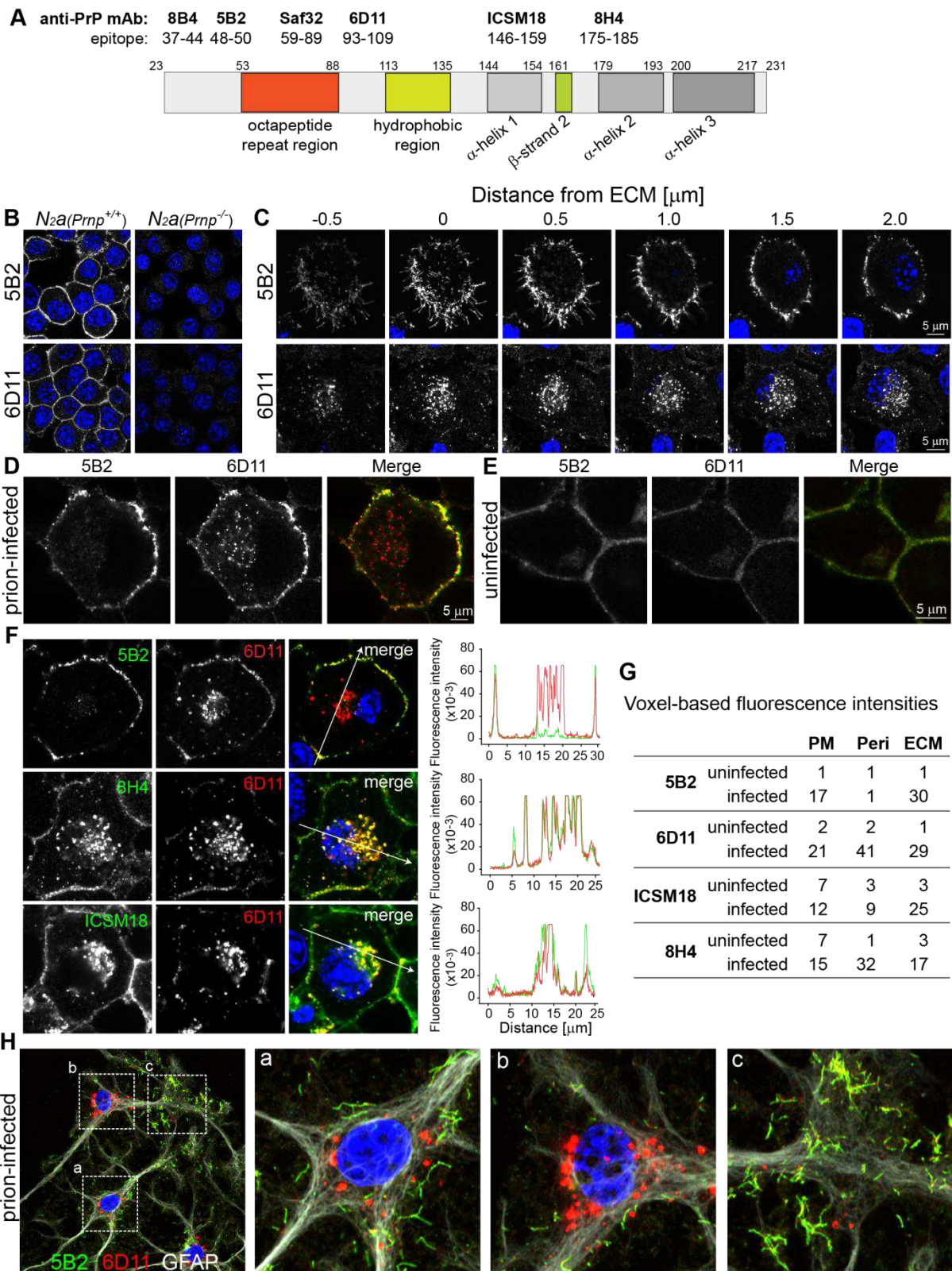
- 788 7. Yim YI, Park BC, Yadavalli R, Zhao X, Eisenberg E, Greene LE. The multivesicular body is the
789 major internal site of prion conversion. *J Cell Sci*, (2015).
- 790
- 791 8. Caughey B, Raymond GJ, Ernst D, Race RE. N-terminal truncation of the scrapie-associated
792 form of PrP by lysosomal protease(s): implications regarding the site of conversion of PrP to
793 the protease-resistant state. *J Virol* **65 No 12**, 6597-6603 (1991).
- 794
- 795 9. Borchelt DR, Taraboulos A, Prusiner SB. Evidence for synthesis of scrapie prion proteins in
796 the endocytic pathway. *J Biol Chem* **267**, 16188-16199 (1992).
- 797
- 798 10. Magalhaes AC, *et al.* Uptake and neuritic transport of scrapie prion protein coincident with
799 infection of neuronal cells. *J Neurosci* **25**, 5207-5216 (2005).
- 800
- 801 11. Barmada SJ, Harris DA. Visualization of prion infection in transgenic mice expressing green
802 fluorescent protein-tagged prion protein. *J Neurosci* **25**, 5824-5832 (2005).
- 803
- 804 12. Dron M, Dandoy-Dron F, Salamat MK, Laude H. Proteasome inhibitors promote the
805 sequestration of PrP^{Sc} into aggresomes within the cytosol of prion-infected CAD neuronal
806 cells. *J Gen Virol*, (2009).
- 807
- 808 13. Goold R, *et al.* Rapid cell-surface prion protein conversion revealed using a novel cell system.
809 *Nat Commun* **2**, 281 (2011).
- 810
- 811 14. Rouvinski A, *et al.* Live imaging of prions reveals nascent PrP^{Sc} in cell-surface, raft-associated
812 amyloid strings and webs. *J Cell Biol* **204**, 423-441 (2014).
- 813
- 814 15. Yamasaki T, Suzuki A, Shimizu T, Watarai M, Hasebe R, Horiuchi M. Characterization of
815 intracellular localization of PrP(Sc) in prion-infected cells using a mAb that recognizes the
816 region consisting of aa 119-127 of mouse PrP. *J Gen Virol* **93**, 668-680 (2012).
- 817
- 818 16. DeArmond SJ, McKinley MP, Barry RA, Braunfeld MB, McColloch JR, Prusiner SB.
819 Identification of prion amyloid filaments in scrapie-infected brain. *Cell* **41**, 221-235 (1985).
- 820
- 821 17. Wenborn A, *et al.* A novel and rapid method for obtaining high titre intact prion strains from
822 mammalian brain. *Sci Rep* **5**, 10062 (2015).
- 823
- 824 18. Terry C, *et al.* Ex vivo mammalian prions are formed of paired double helical prion protein
825 fibrils. *Open Biol* **6**, (2016).
- 826
- 827 19. Bradbury ARM, *et al.* When monoclonal antibodies are not monospecific: Hybridomas
828 frequently express additional functional variable regions. *Mabs* **10**, 539-546 (2018).
- 829
- 830 20. Taraboulos A, Serban D, Prusiner SB. Scrapie prion proteins accumulate in the cytoplasm of
831 persistently infected cultured cells. *J Cell Biol* **110**, 2117-2132 (1990).

- 832
833 21. Veith NM, Plattner H, Stuermer CA, Schulz-Schaeffer WJ, Burkle A. Immunolocalisation of
834 PrP(Sc) in scrapie-infected N2a mouse neuroblastoma cells by light and electron microscopy.
835 *Eur J Cell Biol*, (2008).
- 836
837 22. Prusiner SB. Novel proteinaceous infectious particles cause scrapie. *Science* **216**, 136-144
838 (1982).
- 839
840 23. Ishidoh K, Kominami E. Processing and activation of lysosomal proteinases. *Biol Chem* **383**,
841 1827-1831 (2002).
- 842
843 24. Bowman EJ, Siebers A, Altendorf K. Bafilomycins: a class of inhibitors of membrane ATPases
844 from microorganisms, animal cells, and plant cells. *Proc Natl Acad Sci U S A* **85**, 7972-7976
845 (1988).
- 846
847 25. Man WK, *et al.* The docking of synaptic vesicles on the presynaptic membrane induced by a-
848 synuclein is modulated by lipid composition. *Nat Commun* **12**, 927 (2021).
- 849
850 26. Zhang J, Xue R, Ong WY, Chen P. Roles of cholesterol in vesicle fusion and motion. *Biophys J*
851 **97**, 1371-1380 (2009).
- 852
853 27. Shyng S-L, Moulder KL, Lesko A, Harris DA. The N-terminal domain of a glycolipid-anchored
854 prion protein is essential for its endocytosis via clathrin-coated pits. *J Biol Chem* **270**, 14793-
855 14800 (1995).
- 856
857 28. Sunyach C, *et al.* The mechanism of internalization of glycosylphosphatidylinositol-anchored
858 prion protein. *EMBO J* **22**, 3591-3601 (2003).
- 859
860 29. Macia E, Ehrlich M, Massol R, Boucrot E, Brunner C, Kirchhausen T. Dynasore, a cell-
861 permeable inhibitor of dynamin. *Dev Cell* **10**, 839-850 (2006).
- 862
863 30. Hill TA, *et al.* Inhibition of dynamin mediated endocytosis by the dynoles--synthesis and
864 functional activity of a family of indoles. *J Med Chem* **52**, 3762-3773 (2009).
- 865
866 31. Declercq J, Meulemans S, Plets E, Creemers JW. Internalization of proprotein convertase PC7
867 from plasma membrane is mediated by a novel motif. *J Biol Chem* **287**, 9052-9060 (2012).
- 868
869 32. Grinstein S, Rotin D, Mason MJ. Na⁺/H⁺ exchange and growth factor-induced cytosolic pH
870 changes. Role in cellular proliferation. *Biochim Biophys Acta* **988**, 73-97 (1989).
- 871
872 33. Cerny J, *et al.* The small chemical vacuolin-1 inhibits Ca⁽²⁺⁾-dependent lysosomal exocytosis
873 but not cell resealing. *EMBO Rep* **5**, 883-888 (2004).
- 874

- 875 34. Yamasaki T, Baron GS, Suzuki A, Hasebe R, Horiuchi M. Characterization of intracellular
876 dynamics of inoculated PrP-res and newly generated PrP(Sc) during early stage prion
877 infection in Neuro2a cells. *Virology* **450-451**, 324-335 (2014).
- 878
879 35. Thery C, Zitvogel L, Amigorena S. Exosomes: Composition, biogenesis and function. *Nat Rev*
880 *Immunol* **2**, 569-579 (2002).
- 881
882 36. Couzin J. Cell biology - The ins and outs of exosomes. *Science* **308**, 1862-1863 (2005).
- 883
884 37. Fevrier B, *et al.* Cells release prions in association with exosomes. *Proc Natl Acad Sci U S A*
885 **101**, 9683-9688 (2004).
- 886
887 38. Zahn R. The Octapeptide Repeats in Mammalian Prion Protein Constitute a pH-dependent
888 Folding and Aggregation Site. *J Mol Biol* **334**, 477-488 (2003).
- 889
890 39. Frankenfield KN, Powers ET, Kelly JW. Influence of the N-terminal domain on the aggregation
891 properties of the prion protein. *Protein Sci* **14**, 2154-2166 (2005).
- 892
893 40. Trevitt CR, *et al.* N-terminal Domain of Prion Protein Directs its Oligomeric Association. *J Biol*
894 *chem* **289**, 25497-25508 (2014).
- 895
896 41. Chernoff YO, Lindquist SL, Ono B, Inge Vechtomov SG, Liebman SW. Role of the chaperone
897 protein Hsp104 in propagation of the yeast prion-like factor [psi+]. *Science* **268**, 880-884
898 (1995).
- 899
900 42. Shorter J, Lindquist S. Hsp104 Catalyzes Formation and Elimination of Self-Replicating Sup35
901 Prion Conformers
902 7. *Science*, (2004).
- 903
904 43. Silveira JR, *et al.* The most infectious prion protein particles. *Nature* **437**, 257-261 (2005).
- 905
906 44. Vanni I, *et al.* Isolation of infectious, non-fibrillar and oligomeric prions from a genetic prion
907 disease. *Brain* **143**, 1512-1524 (2020).
- 908
909 45. Harris DA, Huber MT, Van Dijken P, Shyng S-L, Chait BT, Wang R. Processing of a cellular
910 prion protein: identification of N- and C-terminal cleavage sites. *Biochemistry* **32**, 1009-1016
911 (1993).
- 912
913 46. Chen SG, Teplow DB, Parchi P, Teller JK, Gambetti P, Autilio-Gambetti L. Truncated forms of
914 the human prion protein in normal brain and in prion diseases. *J Biol Chem* **270**, 19173-
915 19180 (1995).
- 916

- 917 47. Zanusso G, *et al.* Identification of distinct N-terminal truncated forms of prion protein in
918 different Creutzfeldt-Jakob disease subtypes. *J Biol chem*, (2004).
- 919
920 48. Laffont-Proust I, *et al.* Truncated PrP(c) in mammalian brain: interspecies variation and
921 location in membrane rafts. *Biol Chem* **387**, 297-300 (2006).
- 922
923 49. Parchi P, Strammiello R, Giese A, Kretzschmar H. Phenotypic variability of sporadic human
924 prion disease and its molecular basis: past, present, and future. *Acta Neuropathol*, (2010).
- 925
926 50. Horiuchi M, Caughey B. Prion protein interconversions and the transmissible spongiform
927 encephalopathies. *Structure with Folding & Design* **7**, R231-R240 (1999).
- 928
929 51. Dannies PS. Protein hormone storage in secretory granules: mechanisms for concentration
930 and sorting. *Endocr Rev* **20**, 3-21 (1999).
- 931
932 52. Maji SK, *et al.* Functional amyloids as natural storage of peptide hormones in pituitary
933 secretory granules. *Science* **325**, 328-332 (2009).
- 934
935 53. Nespovitaya N, Gath J, Barylyuk K, Seuring C, Meier BH, Riek R. Dynamic Assembly and
936 Disassembly of Functional beta-Endorphin Amyloid Fibrils. *J Am Chem Soc* **138**, 846-856
937 (2016).
- 938
939 54. Jacob RS, *et al.* Amyloid formation of growth hormone in presence of zinc: Relevance to its
940 storage in secretory granules. *Sci Rep* **6**, 23370 (2016).
- 941
942 55. Mallucci GR. Prion neurodegeneration: Starts and stops at the synapse. *Prion* **3**, (2009).
- 943
944 56. Marbiah MM, *et al.* Identification of a gene regulatory network associated with prion
945 replication. *EMBO J*, e201387150 (2014).
- 946
947 57. Philiastides A, Ribes JM, Yip DC, Schmidt C, Benilova I, Klohn PC. A New Cell Model for
948 Investigating Prion Strain Selection and Adaptation. *Viruses* **11**, (2019).
- 949
950 58. Klohn P, Stoltze L, Flechsig E, Enari M, Weissmann C. A quantitative, highly sensitive cell-
951 based infectivity assay for mouse scrapie prions. *Proc Natl Acad Sci USA* **100**, 11666-11671
952 (2003).
- 953
954 59. Schmidt C, *et al.* A systematic investigation of production of synthetic prions from
955 recombinant prion protein. *Open Biol* **5**, 150165 (2015).
- 956
957 60. Costes SV, Daelemans D, Cho EH, Dobbin Z, Pavlakis G, Lockett S. Automatic and quantitative
958 measurement of protein-protein colocalization in live cells. *Biophys J* **86**, 3993-4003 (2004).
- 959

- 960 61. Ran FA, Hsu PD, Wright J, Agarwala V, Scott DA, Zhang F. Genome engineering using the
961 CRISPR-Cas9 system. *Nat Protoc* **8**, 2281-2308 (2013).
- 962
963 62. Riek R, Hornemann S, Wider G, Billeter M, Glockshuber R, Wuthrich K. NMR structure of the
964 mouse prion protein domain PrP (121-231). *Nature* **382**, 180-182 (1996).
- 965
966 63. Li RL, *et al.* Identification of an epitope in the C terminus of normal prion protein whose
967 expression is modulated by binding events in the N terminus. *Journal of Molecular Biology*
968 **301**, 567-573 (2000).
- 969
970 64. Lauren J, Gimbel DA, Nygaard HB, Gilbert JW, Strittmatter SM. Cellular prion protein
971 mediates impairment of synaptic plasticity by amyloid-beta oligomers. *Nature* **457**, 1128-
972 1132 (2009).
- 973
974 65. Antonyuk SV, *et al.* Crystal structure of human prion protein bound to a therapeutic
975 antibody. *Proceedings of the National Academy of Sciences of the United States of America*
976 **106**, 2554-2558 (2009).
- 977
978 66. Pan T, Li R, Kang SC, Wong BS, Wisniewski T, Sy MS. Epitope scanning reveals gain and loss of
979 strain specific antibody binding epitopes associated with the conversion of normal cellular
980 prion to scrapie prion. *J Neurochem* **90**, 1205-1217 (2004).
- 981
982 67. Kang M, Yeon KS, An SS, Ran JY. Characterizing affinity epitopes between prion protein and
983 beta-amyloid using an epitope mapping immunoassay. *Exp Mol Med* **45**, e34 (2013).
- 984
985 68. Zanusso G, *et al.* Prion protein expression in different species: analysis with a panel of new
986 mAbs. *Proc Natl Acad Sci U S A* **95**, 8812-8816 (1998).
- 987
988 69. Silva CJ. Using small molecule reagents to selectively modify epitopes based on their
989 conformation. *Prion* **6**, (2012).
- 990
991 70. Katorcha E, Makarava N, Savtchenko R, Azzo D, Baskakov IV. Sialylation of Prion Protein
992 Controls the Rate of Prion Amplification, the Cross-Species Barrier, the Ratio of PrPSc
993 Glycoform and Prion Infectivity. *PLoS Pathog* **10**, e1004366 (2014).
- 994
995 71. Faris R, *et al.* Cellular prion protein is present in mitochondria of healthy mice. *Sci Rep* **7**,
996 41556 (2017).
- 997
998 72. Sauer H, Dagdanova A, Hescheler J, Wartenberg M. Redox-regulation of intrinsic prion
999 expression in multicellular prostate tumor spheroids. *Free Radical Biology and Medicine* **27**,
1000 1276-1283 (1999).
- 1001
1002 73. Demart S, *et al.* New insight into abnormal prion protein using monoclonal antibodies.
1003 *Biochem Biophys Res Commun* **265**, 652-657 (1999).



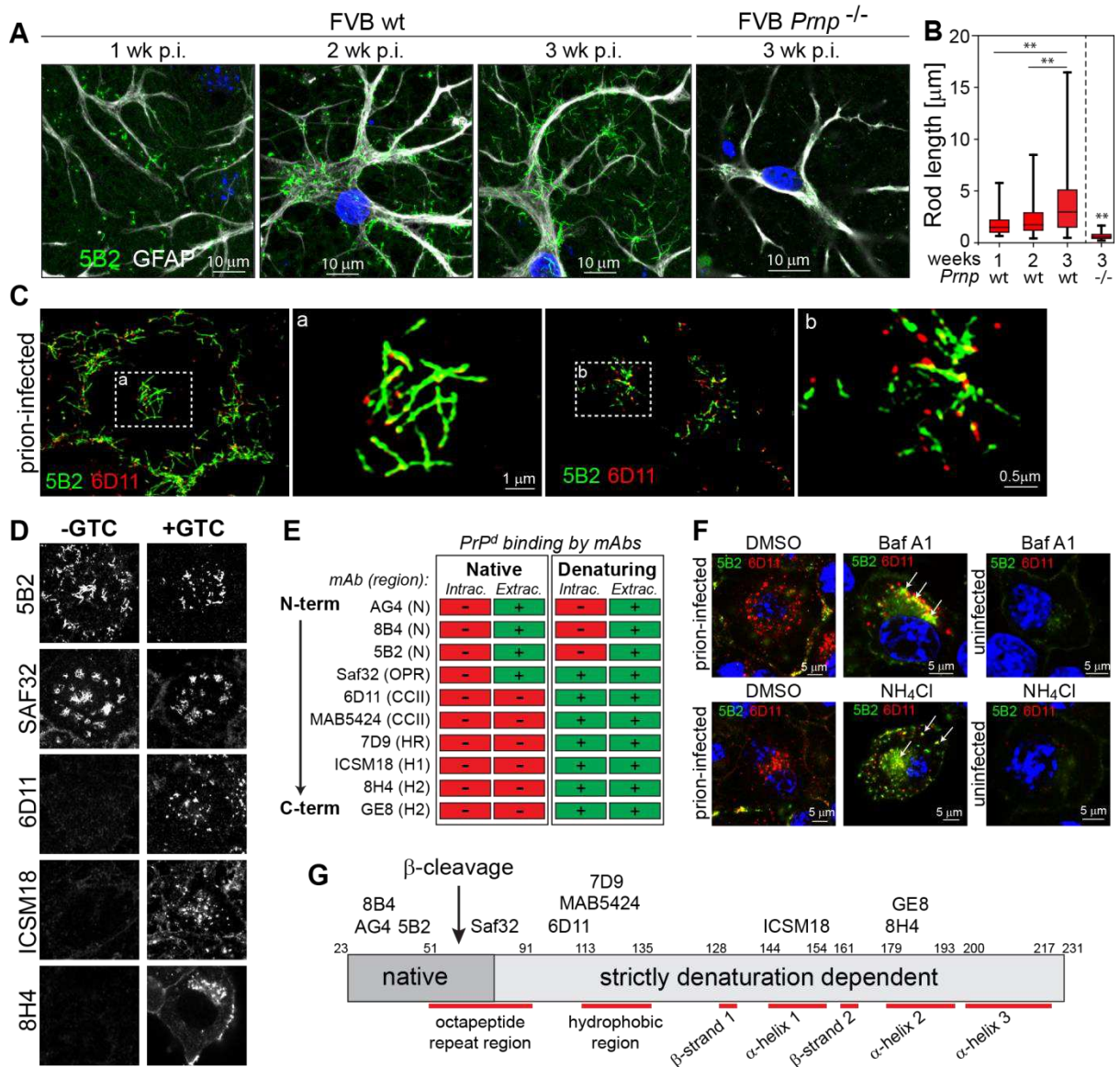
1004

1005 **Fig. 1: Identification of phenotypically distinct PrP^d aggregates in prion-infected cells**
 1006 **using monospecific anti-PrP mAbs**

1007 (A) Schematic diagram of validated anti-PrP mAbs and their putative epitopes on the context
 1008 of mouse PrP domains⁶².

1009 (B) Exemplary data for anti-PrP mAb validation using N2a (*Prnp^{-/-}*) wild-type (*Prnp^{+/+}*) cells.
 1010 For full data set of anti-PrP mAbs tested see Fig. S1A.

1011 (C) Serial confocal sections of prion-infected S7 cells, labelled with anti-PrP mAbs 5B2 and
1012 6D11, respectively. Cells were grown for extended cultures times, i.e. 6 days.
1013 (D, E) Co-labelling of prion-infected (D) and uninfected control (E) cells with 5B2 and 6D11.
1014 (F) Detection of perinuclear PrP^d by core, but not by N-terminal anti-PrP mAbs in prion-
1015 infected cells. Arrows in merged images depict orientation and placement of fluorescence
1016 intensity profiles, shown at the right hand side of image panels. For complete data set with
1017 all monospecific mAbs see Fig. S2.
1018 (G) MAb-dependent differences in the detection of PrP^d versus PrP^c, mapped as normalised
1019 voxel-based intensities in cellular loci where PrP^d deposits (PM: plasma membrane; Peri:
1020 perinuclear region; ECM: extracellular matrix). For data see Table S2.
1021 (H) Primary neuronal cultures from embryonic e17 mouse brains, infected with a 10⁻⁵ dilution
1022 of the prion strain 22L (10% brain homogenate, w/v), triple-labelled with 5B2, 6D11 and anti-
1023 GFAP.
1024



1025

1026

1027

Fig. 2: Elongation and structural features of fibril-like PrP^d aggregates and crypticity of PrP^d epitopes

1028 (A) Time-dependent growth of 5B2-positive PrP^d fibrils in primary astrocytes of FVB-wt
1029 (*Prnp*^{+/+}), but not in those of FVB-ko (*Prnp*^{-/-}) mice, following infection with RML.

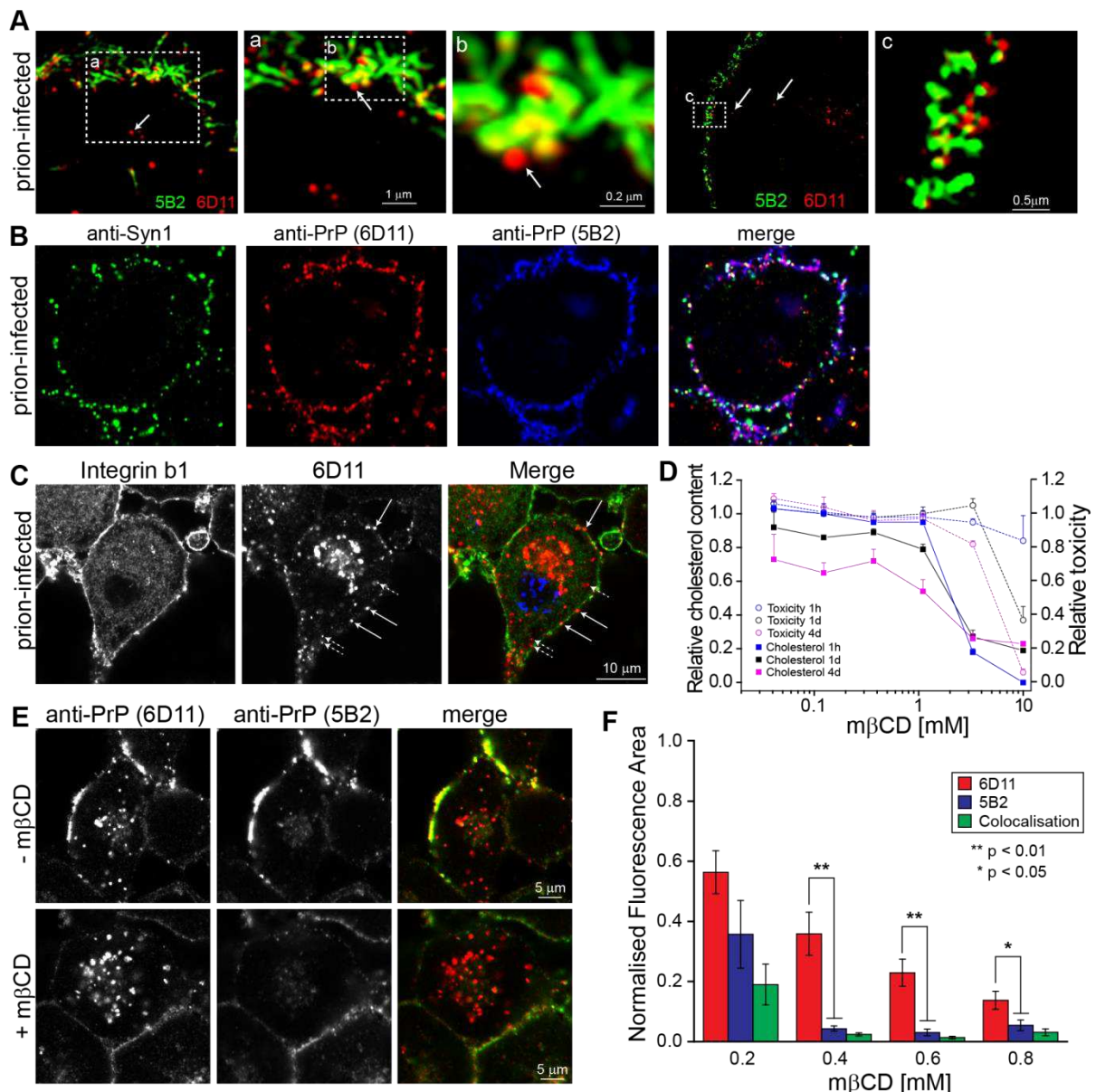
1030 (B) Lengths of fibril-like PrP^d aggregates in FVB-wt versus FVB-ko mice. Significance levels
1031 for time-dependent fibril growth in FVB-wt (*Prnp*^{+/+}) mice and for FVB-wt versus FVB-ko were
1032 assessed by Kruskal-Wallis test with Dunn's multiple comparisons with ** *p*<0.001.

1033 (C) SIM images of fibril-like PrP^d aggregates at the ECM of prion-infected S7 cells, labelled
1034 with 5B2 and 6D11 after GTC treatment. Magnified area (a) and (b) denoted by dashed box.
1035 (D) Identification of cryptic epitopes in PrP^d-bearing cells. Prion-infected cells were incubated
1036 with anti-PrP mAbs in absence and presence of GTC. For complete image data set see Fig.
1037 S4.

1038 (E) Summary of anti-PrP mAb binding to PrP^d aggregates under native (-GTC) and
1039 denaturing (+GTC) conditions with corresponding PrP domains (for abbreviations of PrP
1040 regions see Fig. S4).

1041 (F) Detection of intracellular 5B2-positive PrP^d aggregates following a 16h incubation with
1042 6nM BafA1 and 16 mM NH₄Cl, respectively.

1043 (G) Model depicting cryptic, exposed and putative PrP-cleavage sites, respectively (modified
1044 from Rouvinski et al.¹⁴).
1045



1046

1047

1048

1049

1050

1051

1052

1053

1054

1055

1056

1057

1058

1059

1060

1061

1062

1063

Fig. 3: The formation of PrP^d fibrils at the plasma membrane is associated with vesicular trafficking and is sensitive to cholesterol-lowering

(A) SIM images of prion-infected cells, double-labelled with 5B2 and 6D11 at the level of the plasma membrane. Magnified areas a, b and c are denoted by dashed boxes. Arrows denote punctate 6D11-positive PrP^d.

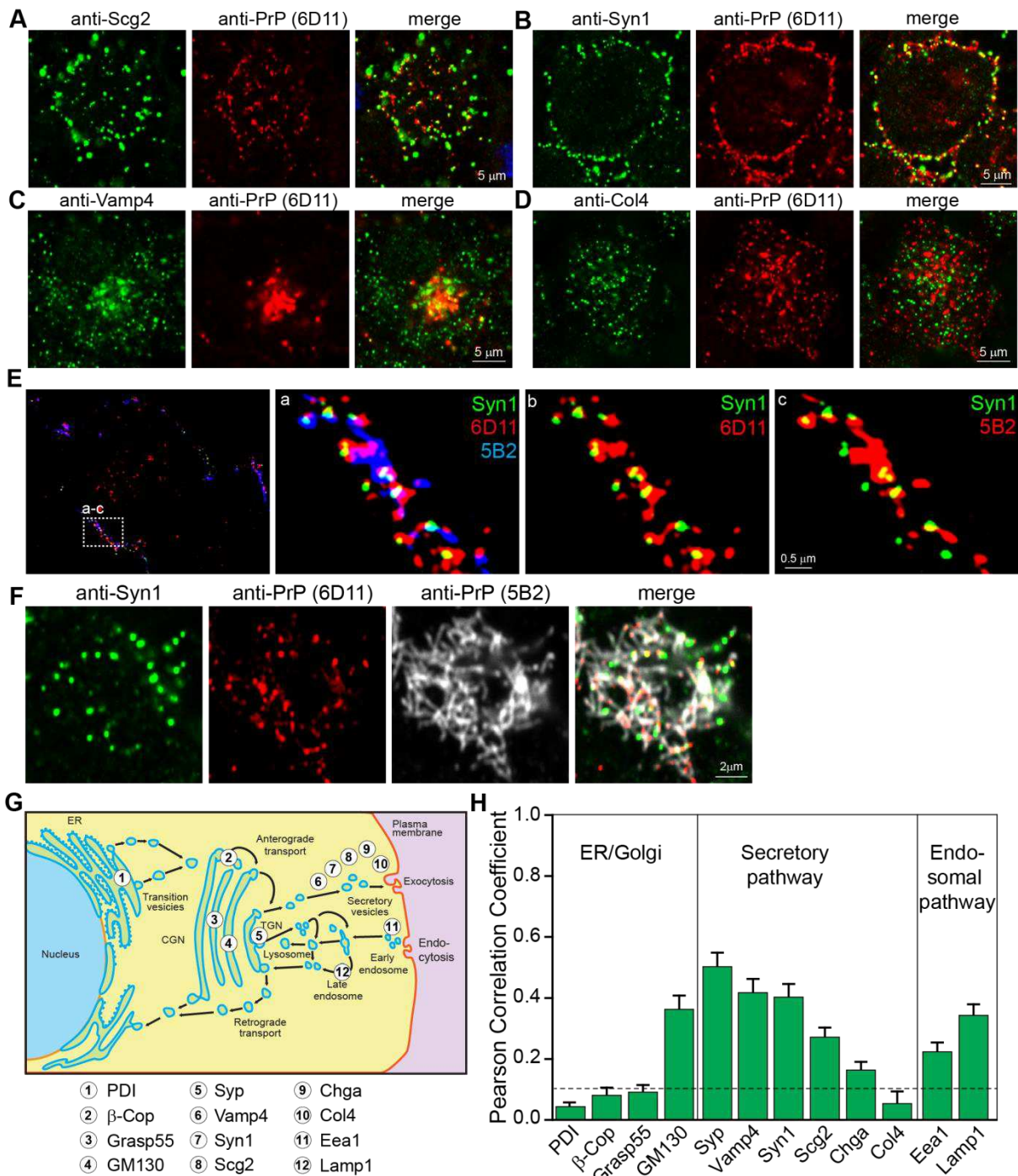
(B) Triple-labelling of prion-infected cells with anti-Syn1, 6D11 and 5B2. A schematic for additive colour mixing was added next to the merged image to depict colocalisation patterns.

(C) Prion-infected cells, labelled with anti-integrin $\beta 1$ and 6D11 show PrP^d aggregates proximal to (short hatched arrows) and at the level of (long straight arrows) the plasma membrane.

(D) Dose-response relationship of m β CD on cholesterol-lowering and toxicity in prion-infected iS7 cells at the time points and m β CD concentrations specified.

(E) Colocalisation of 6D11 and 5B2 at the plasma membrane in presence and absence of 0.4 mM m β CD at 16 hours following m β CD addition.

(F) Quantification of m β CD effects on fluorescence and colocalisation of 6D11 and 5B2 at 16h after addition of specified inhibitor concentrations.



1064

1065

1066

1067

1068

1069

1070

1071

1072

1073

1074

1075

Fig. 4: PrP^d is segregated into exocytotic vesicles of the regulated secretory pathway and colocalises with markers of the endosomal pathway

(A-D) Prion-infected cells were co-labelled with 6D11 and vesicular markers (A) Scg2, (B) Syn1 and (C) Vamp4 as well as with constitutively secreted Col4 (D).

(E) SIM image of plasma membrane, triple-labelled (a) or double-labelled (b, c) with Syn1, 6D11 and 5B2. Magnified areas (a-c) are denoted by a dashed box in the first image.

(F) Triple-labelling with 5B2, 6D11 and anti-Syn1 of PrP^d at the ECM of infected cells.

(G) Diagram of marker proteins used to map trafficking routes of 6D11-positive PrP^d.

(H) Levels of colocalisation, expressed as Pearson correlation coefficients. Representative images and abbreviations are shown in Fig. S5.

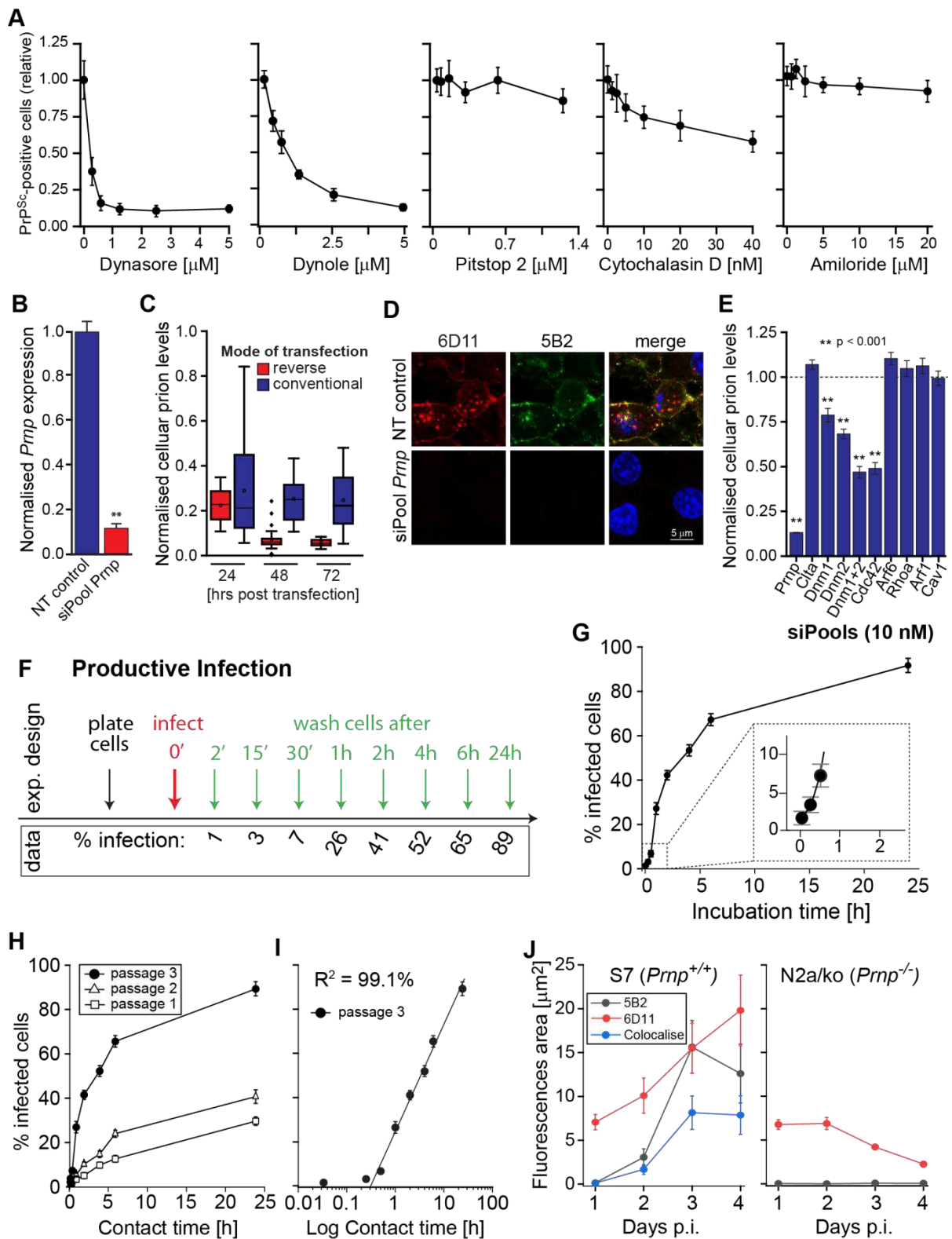
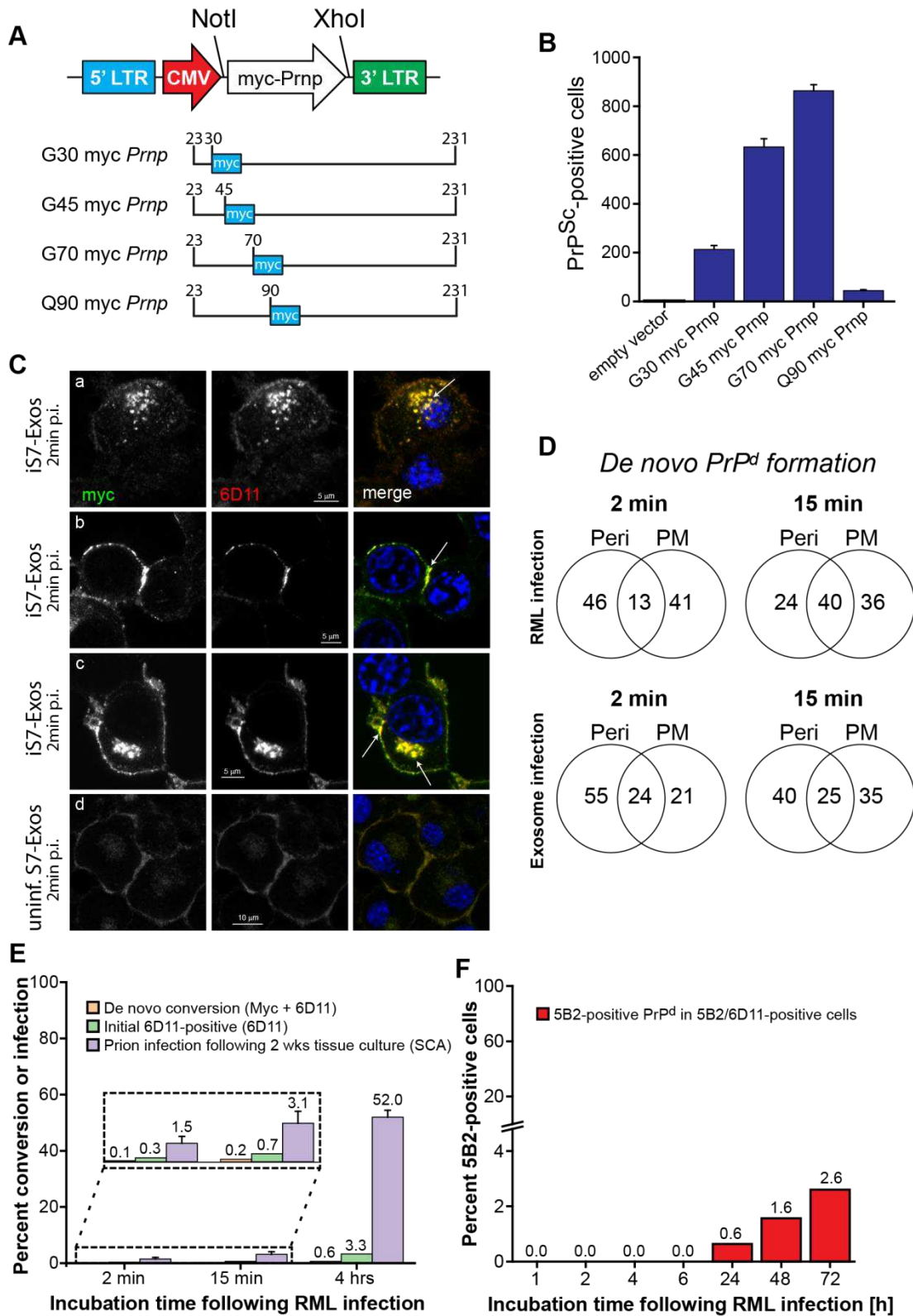


Fig. 5: Identification of PrP^d internalisation pathways and the minimum contact time for productive cell infection

(A) Persistently prion-infected iS7 cells were incubated with endocytosis inhibitors and changes in prion steady state levels were determined by SCA. Mean values \pm SEM of at least three independent experiments are shown. For toxic threshold levels, SCA data and significance levels of all inhibitors see Tables S3 and S4.

1084 (B) Gene silencing of *Prnp* in S7 cells using pooled siRNA, determined by RT-qPCR; mean
1085 values + SD of three independent experiments is shown ($p < 0.01$).
1086 (C) Time-dependent effect of *Prnp* silencing on prion steady state levels following
1087 conventional and reverse transfection of cells.
1088 (D) Effect of *Prnp* knockdown on PrP^d aggregates in chronically infected cells following
1089 reverse transfection with siPools against *Prnp* and a NT control.
1090 (E) Silencing of gene targets associated with endocytic pathways in persistently infected iS7
1091 cells and its effect on prion steady state levels. For knockdown efficacies see **Table S5**.
1092 (F) Schematic for assessing the minimum contact time for productive prion infection of cells.
1093 S7 cells were plated out in parallel and infected with clarified RML homogenates, followed by
1094 gentle washing of cells with PBS at the specified time points to remove inoculum. Cells were
1095 then grown to confluence and the proportion of infected cells was determined by SCA.
1096 (G) Proportion of prion-infected cells, determined by SCA was plotted against contact times
1097 after infection with RML. Insert: magnified area of the proportion of infected cells at early
1098 time points, i.e. 2', 15' and 1h.
1099 (H) Relationship between contact time and the proportion of infected cells following infection
1100 with RML during subsequent cell passages.
1101 (I) Replotted data from (G) as a semi-logarithmic (linear-log) graph.
1102 (J) Prion replication-permissive (S7) and -refractory (N2a/ko) cells were infected with prion-
1103 infected exosomes and the formation of 6D11-, 5B2-positive and double-positive PrP^d was
1104 determined. Data represent average values \pm SD of three independent experiments.
1105



1106

1107

1108 **Fig. 6: Prion infection leads to PrP conversion at two distinct cellular locations and**
 1109 **precedes the formation of FL-PrP^d**

1110 (A) Cloning of N-terminal versions of myc-tagged *Prnp* into the retroviral vector pLNCX2.

1111 The position of insertion of the myc tag is depicted.

1112 (B) Comparative susceptibilities of myc-tagged *Prnp* expressing cells after infection with a
1113 10^{-4} dilution of RML prions (titre: $10^{8.4}$ LD50 units/g). An empty vector confirms that cells
1114 transcriptionally silenced with hairpins against the 3'UTR of *Prnp* are refractory to prion
1115 infection.

1116 (C) G70 PrP-expressing cells, fixed at 2 min following infection with infected exosomes were
1117 colabelled with AF488-conjugated anti-myc and the discriminatory 6D11 mAbs. Detection of
1118 myc PrP^d at distinct cellular locations is depicted by arrows in merged images: perinuclear
1119 (panel a), plasma membrane (panel b), perinuclear and plasma membrane (panel c), mock-
1120 infected control cells (panel d).

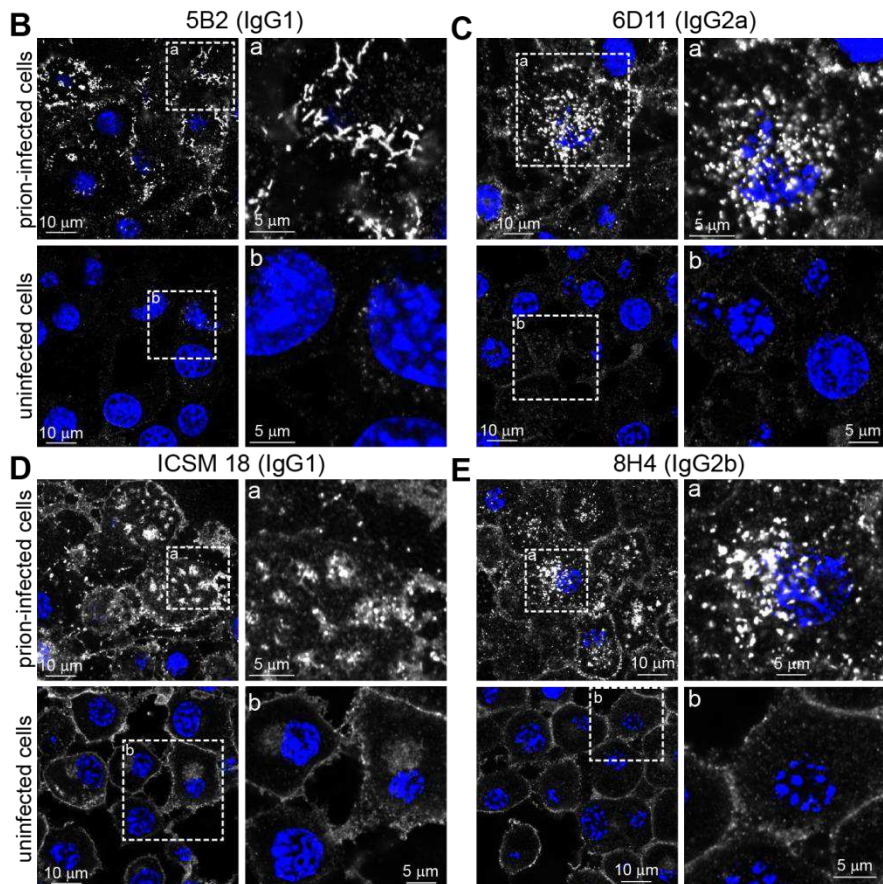
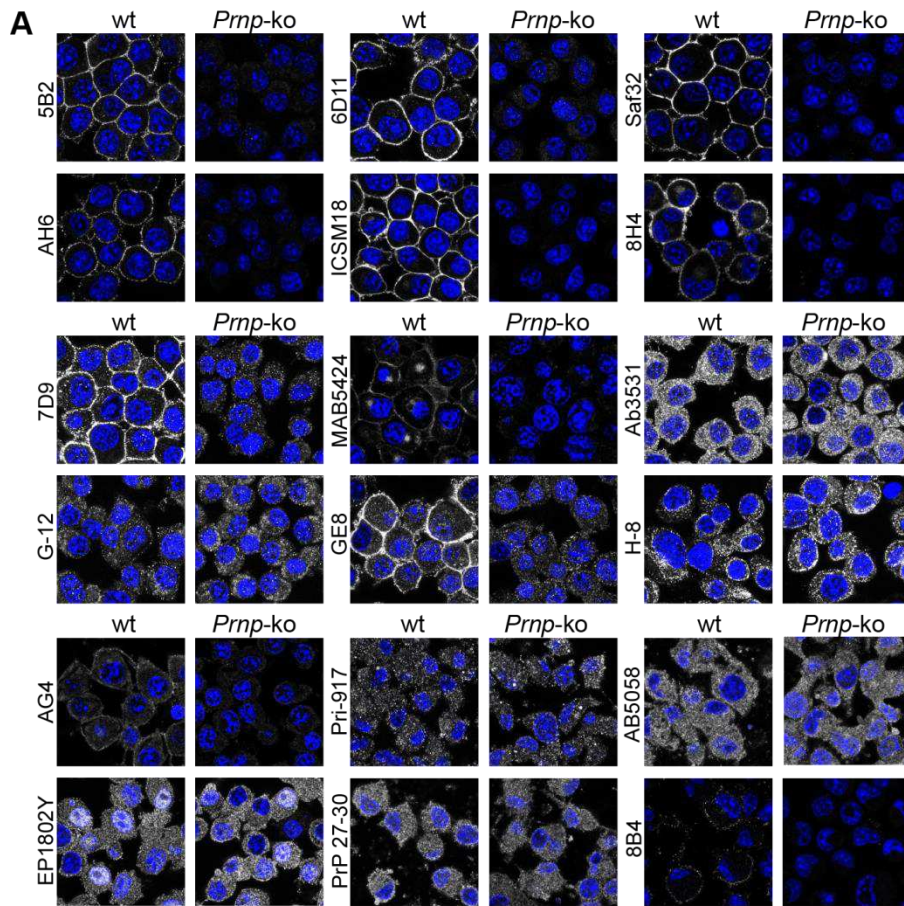
1121 (D) Identifying the cellular sites of *de novo* conversion. Detection of *de novo* converted PrP
1122 in G70 PrP expressing cells at 2 min and 15 min after infection with RML and exosomes at
1123 perinuclear sites (Peri), the plasma membrane (PM), or both sites as represented by Venn
1124 diagrams in percent of total. At least 50 myc PrP^d positive cells were analysed per condition
1125 by three investigators.

1126 (E) Quantitative analysis of contact times against the proportion of cells with evident *de novo*
1127 PrP conversion (Myc + 6D11) and initially infected (6D11) cells, respectively. G70 PrP-
1128 expressing cells were infected with RML for the specified times, gently washed to remove
1129 the inoculum, fixed and labelled. For comparison, the proportion of infected cells after two
1130 weeks of tissue culture following exposure with prions at the specified contact times, data
1131 reblotted from Fig. 6G, are shown (violet bars). Mock-infected background-corrected data
1132 from 81 frames of about 60 cells per frame were scored as specified in Methods.

1133 (F) Relationship between cell contact times after RML infection and the detection of 5B2-
1134 positive FL-PrP^d. G70 PrP-expressing cells were infected with RML for the specified times
1135 as above. Cells were subsequently fixed and labelled with 5B2 and 6D11, followed by
1136 fluorescence conjugated secondary antibodies. As above, the number of double-positive
1137 cells was scored.

1138

1139

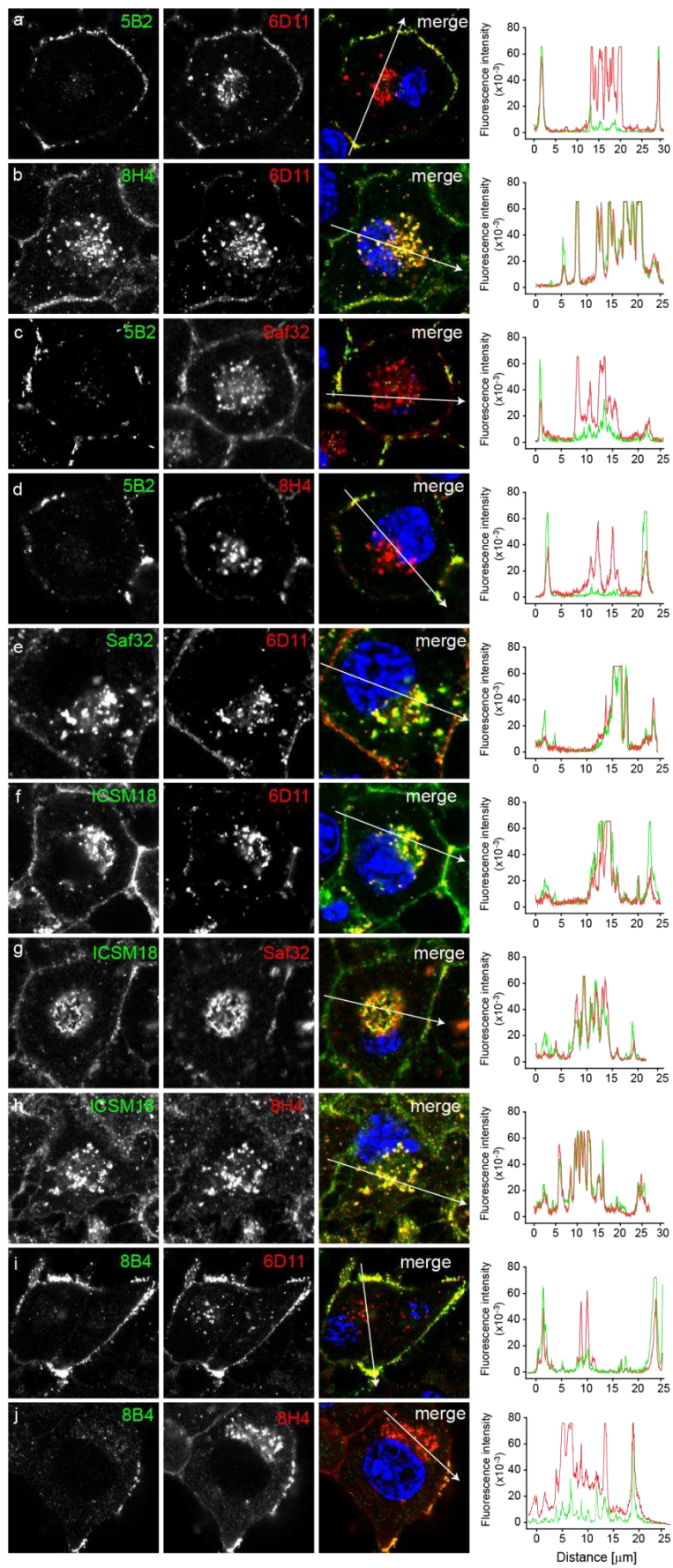


1142 **Fig. S1: Anti-PrP antibody validation and PrP^d phenotypes**

1143 (A) To assess the target specificity of anti-PrP antibodies, *Prnp* was deleted in N₂a cells by
1144 CRISPR-Cas9 as specified in Methods. Aliquots of N₂a (wt) and N₂a-*Prnp*^{-/-} (*Prnp*-ko) cells
1145 were plated into wells of 8-well chamber slides at a concentration of 5 x 10⁴ cells/ml OFCS.
1146 After three days of culture, cells were fixed with 3.7% formalin for 12 minutes, washed once
1147 with PBS and permeabilised with 0.04% Triton X-100 for 10 minutes. Cells were incubated at
1148 4° C overnight with primary anti-PrP antibodies in Superblock. After washing with PBS, cells
1149 were labelled with AF488-conjugated anti-mouse IgG (H+L) at a 1:1,000 dilution overnight at
1150 4° C. All images were acquired with the same photomultiplier tube (PMT) gain to account for
1151 differences in labelling intensities.

1152 (B-E) Phenotypic differences of PrP^d aggregates detected with distinct anti-PrP mAbs.
1153 Chronically prion-infected (upper panels) and uninfected (lower panels) cells were fixed and
1154 denatured according to Methods and labelled with anti-PrP antibodies 5B2 (A), 6D11 (B),
1155 ICSM18 (C) and 8H4 (D), followed by AF488-conjugated secondary antibodies and DAPI for
1156 nuclei. Panels a and b represent magnifications and are denoted in the left panels by
1157 dashed inserts. All images were acquired with the same photomultiplier tube (PMT) gain to
1158 account for antibody-dependent differences in fluorescence intensities.

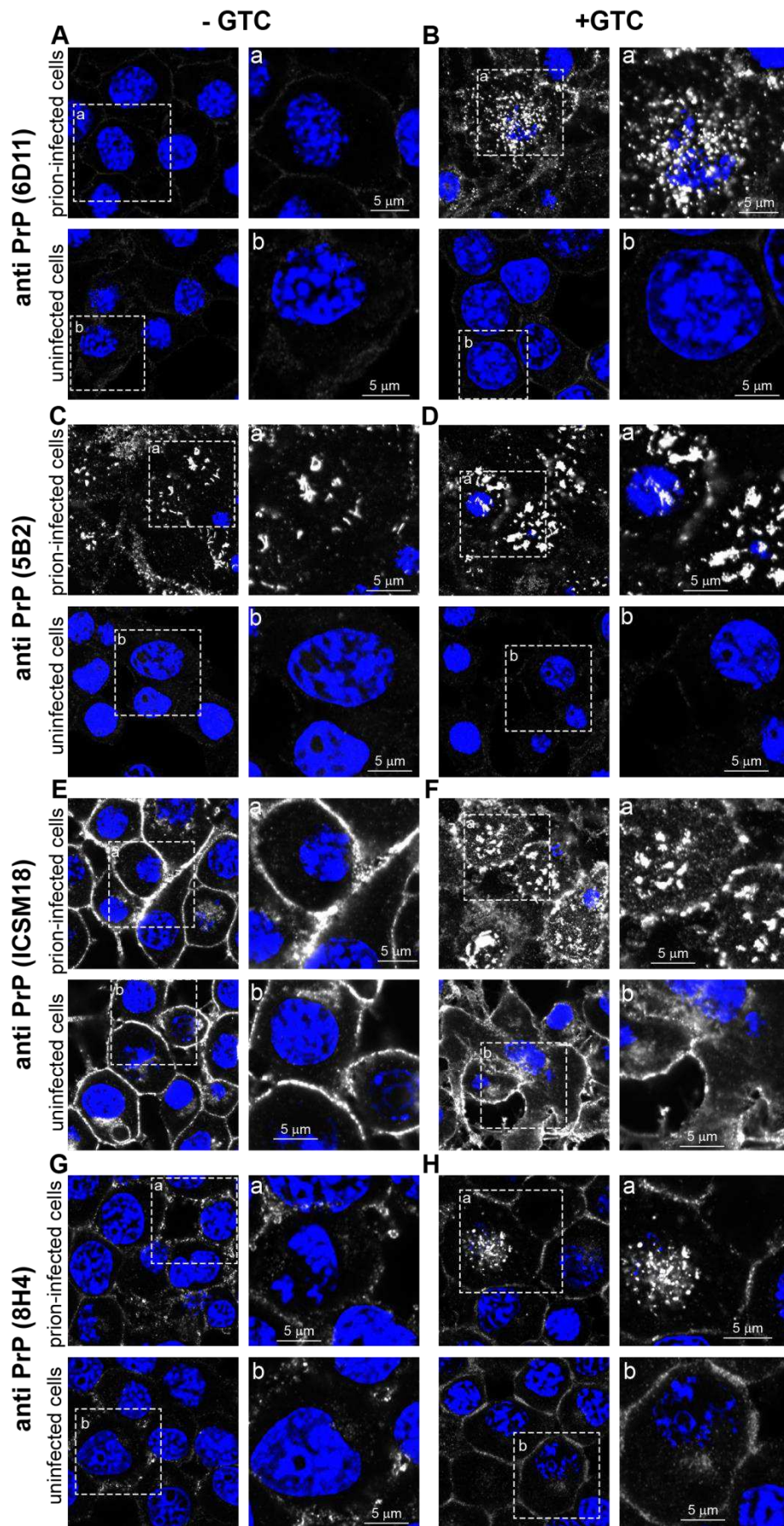
1159

A

1160

1161

1162 **Fig. S2: Antibodies against the N-terminal region of PrP fail to label perinuclear**
1163 **deposits of PrP^d**
1164 Aliquots of 5×10^4 persistently prion-infected iS7 cells per ml OFCS were plated out into
1165 wells of 8-well chamber slides and cultured for 4 days. After fixation and denaturation with
1166 3.5 M GTC as specified in Methods, cells were labelled overnight with the specified primary
1167 antibodies. After washing with PBS, cells were labelled overnight with isotype-specific
1168 fluorescence-conjugated antibodies (AffiniPure, Jackson ImmunoResearch). Note that all
1169 pairwise mAb combinations displayed have different antibody isotypes, i.e. IgG1 (5B2,
1170 ICSM18, 8B4), IgG2a (6D11) and IgG2b (8H4, Saf32), while mAbs with the same isotype
1171 could not be used for co-labelling. Arrows in images “merge” depict the orientation and
1172 placement of fluorescence intensity profiles, shown on the right hand side of image panels.
1173

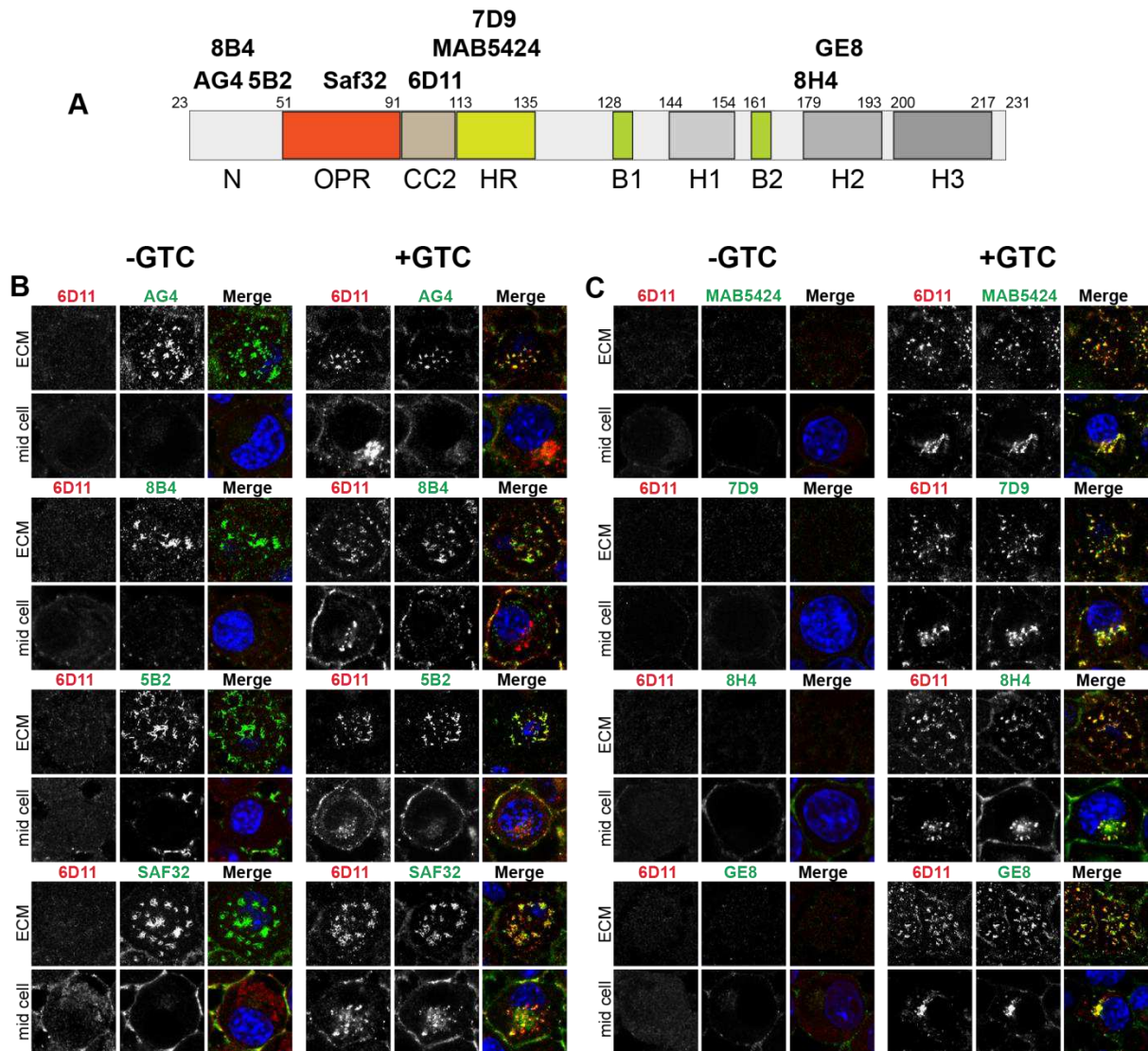


1174

1175

1176 **Fig. S3: Identification of cryptic epitopes in PrP^d aggregates**

1177 (A-H) Confluent layers of prion-infected iS7 (top panel) and uninfected S7 (bottom panel)
1178 cells were fixed, permeabilised and incubated for 10 minutes with PBS (A, C, E, G) and 3.5
1179 M GTC (B, D, F, H), respectively. Cells were then immunolabelled overnight with primary
1180 mAbs 6D11 (A, B), 5B2 (C, D), ICSM 18 (E, F) and 8H4 (G, H), followed by incubation with
1181 AF488-conjugated secondary antibody (IgG (H+L), Jackson ImmunoResearch). Hatched
1182 inserts denote magnified areas which are displayed on the right of the original image.
1183

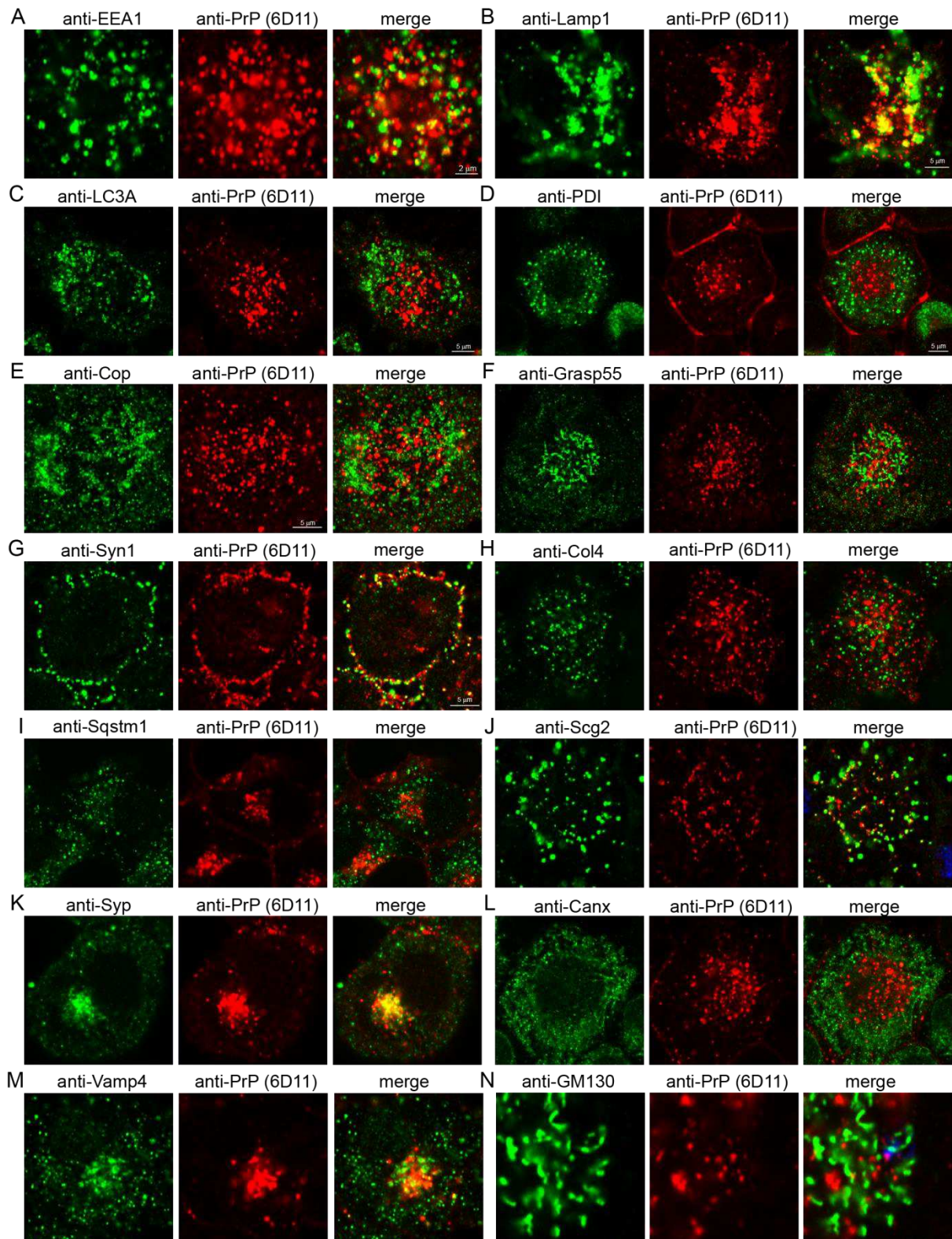


1184

1185 **Fig. S4: Binding of N-terminal and core anti-PrP mAbs to aggregated PrP^d under**
 1186 **native and denaturing conditions**

1187 (A) Schematic diagram of anti-PrP mAbs used in this figure and their epitopes on the context
 1188 of mouse PrP domains, abbreviated as follows: N: N-terminus, OPR: octapeptide repeat
 1189 region, CC2: charge cluster 2, HR: hydrophobic region, B1: β -strand 1, H1: α -helix 1, B2: β -
 1190 strand 2, H2: α -helix 2, H3: α -helix 3. MAbs with minor off-target effects were included where
 1191 detection of aggregated PrP^d showed significantly higher fluorescence than that of PrP^c.
 1192 (B, C) Prion-infected iS7 cells were fixed with formalin and treated with 3.5 M GTC and PBS,
 1193 respectively. Cells were then double-labelled with the discriminatory mAb 6D11 as a
 1194 reference and with any one of the following mAbs: (B) AG4, 8B4, 5B2 and Saf32 and (C)
 1195 MAB5424, 7D9, 8H4 and GE8. After labelling overnight, cells were washed twice and
 1196 labelled with isotype-specific secondary antibodies. PrP^d binding of mAbs was imaged at two
 1197 distinct focal levels, ECM and "mid cell". At mid cell level, perinuclear sites as well as plasma
 1198 membranes are clearly visible. The two focal levels thus include all sites where PrP^d
 1199 deposits were detected, i.e. the plasma membrane, perinuclear sites and the ECM.
 1200 Representative single cell images are shown.

1201

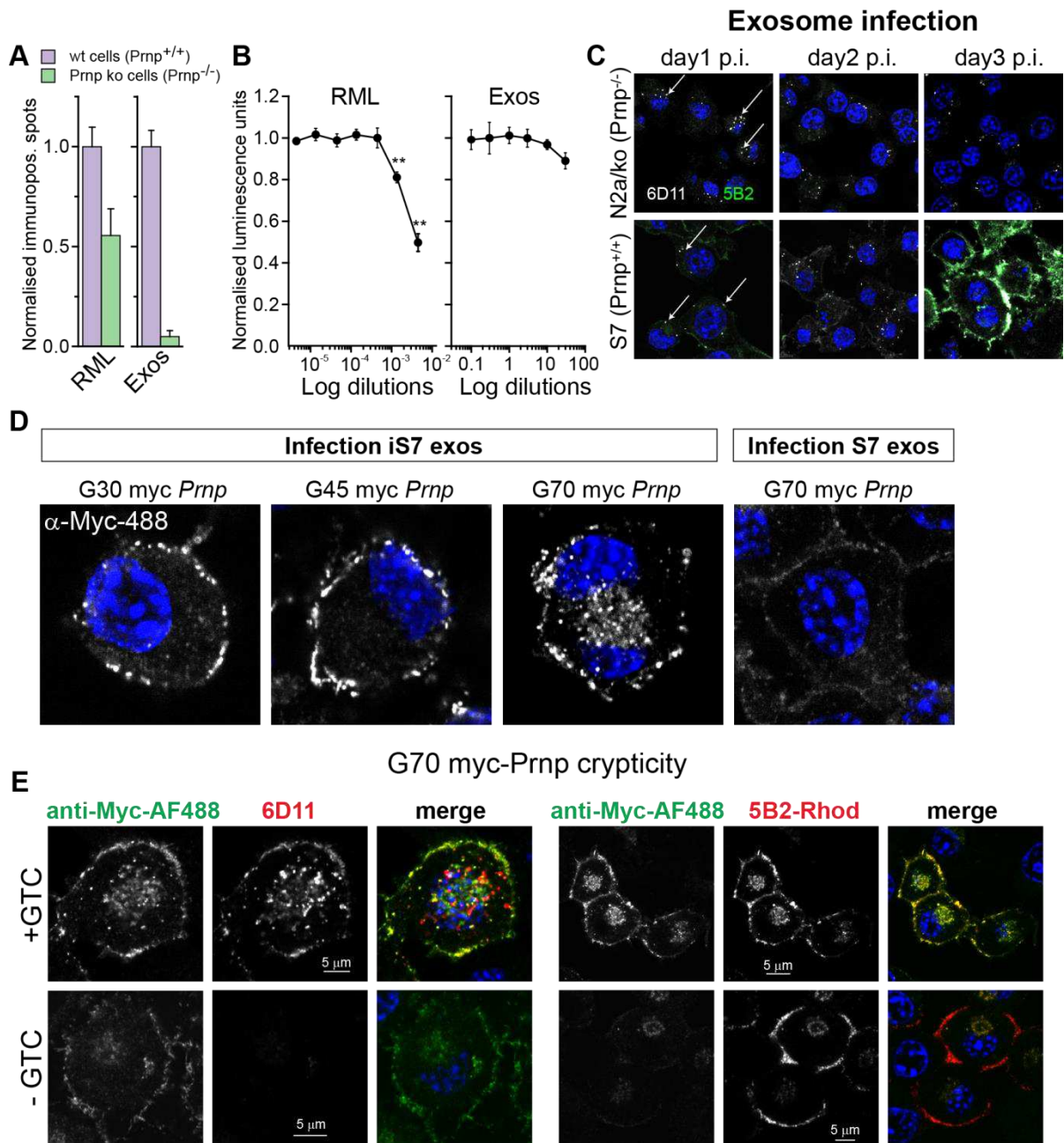


1202

1203 **Fig. S5: Identification of overlapping distributions of PrP^d with organelle markers to**
 1204 **map intracellular trafficking routes of PrP^d**

1205 (A-N) Chronically prion-infected cells were fixed and processed according to Materials and
 1206 Methods and labelled with the specified primary antibodies. Following washing with PBS
 1207 highly cross-adsorbed fluorescence-conjugated secondary antibodies (AffiniPure, Jackson
 1208 ImmunoResearch Laboratories) were incubated overnight at a dilution of 1:1,000
 1209 PBS/Superblock (4:1). Representative images are shown. Corresponding Pearson

1210 correlation coefficients are shown in Fig. 4H. Organelle markers used: (A) Eea1: Early
1211 endosome antigen 1 (B) Lamp1: Lysosomal associated membrane protein 1 (C) LC3A/
1212 MAP1LC3A: Microtubule Associated Protein 1 Light Chain 3 Alpha (D): Pdi/P4hb: Protein
1213 disulphide isomerase (E): β -Cop/Copb1: Coatomer protein complex subunit beta 1 (F):
1214 Grasp55/Gorasp2: Golgi reassembly stacking protein (G) Syn1: Synapsin 1 (H) Col4:
1215 Collagen 4 (I) Sqstm1: Sequestosome 1 (J): Scg2: Secretogranin 2 (K) Syp: Synaptophysin
1216 (L) Canx: Calnexin (M) Vamp4: Vesicle-associated membrane protein 4 (N) Gm130/Golga2:
1217 Golgin A2.
1218



1219

1220

1221

1222

1223

1224

1225

1226

1227

1228

1229

1230

1231

1232

1233

1234

Fig. S6: Infection of S7 and G70 *Prnp* expressing cells with prion-infected exosomes
 (A) Prion-susceptible S7 (*Prnp*^{+/+}) cells and prion-refractory N2a/ko (*Prnp*^{-/-}) cells were infected with 7.5×10^5 Tissue culture infectious units (TCIU)/ml RML and infectious exosomes, respectively and the number of 6D11-positive spots was determined 3 days after infection by SCA. Data represents average spot counts \pm SD, normalised to the corresponding spot numbers of S7 cells. Spots in refractory N2a/ko cells represent inoculum background.
 (B) RML and exosome stock solutions, containing 2.3×10^6 TCIU/ml were serially diluted and S7 cells were infected. After 24h toxicity was determined using CellTiter-Glo luminescent cell viability assay. Data represent normalised average luminescent units \pm SD. Significant changes (** $p < 0.001$) were determined using one-way ANOVA.
 (C) Prion-susceptible (S7) and -refractory (N2a/ko) cells were incubated with 30 μ l exosome concentrate/ml medium, corresponding to an infectious titre of $10^{6.36}$ TCIU/ml. After 1-3 days post infection (p.i.) cells were fixed and labelled with 6D11 and 5B2. Arrows depict 6D11-positive PrP^d at the perinuclear region.

1235 (D) Myc PrP-expressing cells, infected with exosomes from persistently infected (iS7) and
1236 uninfected (S7) cells, respectively were cultured for 6 passages after infection, fixed and
1237 labelled with AF488-conjugated anti-Myc antibody. Cells were imaged at mid-cell level to
1238 visualise myc PrP^d at perinuclear sites and the plasma membrane.
1239 (F) Persistently infected G70-*Prnp* expressing cells were grown to confluency in 8-well
1240 chambered glass slides. Following fixation and acetone treatment, cells were incubated for
1241 10 min with 3.5M GTC or PBS. Cells were thoroughly washed with PBS and labelled with
1242 anti-Myc-AF488 and 6D11 (left panel) and with anti-Myc-AF488 and Rho-conjugated 5B2
1243 (right panel). All cells were imaged with the same PMT gains.
1244

1245 **Supplementary Tables**

1246

1247

Name	[†] Mono-specific	PrP epitope ([§] domain)	^{*†} Host, Isotype	^{*†} Vendor, Order #
5B2	+	48–50 ^a (N-term)	M, IgG1	SC, Sc-47730
6D11	+	93–109 ^b (CC2)	M, IgG2a	SC, Sc-58581
ICSM18	+	146–159 ^c (H1)	M, IgG1	MRC, N/A
8H4	+	175–185 ^d (H2)	M, IgG2b	Sigma, P0110
Saf32	+	59–89 ^e (OPR)	M, IgG2b	Cayman, 189720
8B4	+	37–44 ^f (N-term)	M, IgG1	SC, Sc-47729
AH6	+	N/A	M, IgG2a	SC, Sc-69896
AG4	+/-	32-52 ^g (N-term)	M, IgG2b	TSE RC, RC 059
7D9	+/-	112-124 ^g (HR)	M, IgG1	Abcam, ab14219
MAB5424	+/-	105-125 ^b (CC2, HR)	M, IgG1	Merck, MAB5424
GE8	+/-	183-191 ^g (H2)	M, IgG2b	TSE RC, RC 061
ab3531	-	90-102 ^h (CC2)	R, IgG	Abcam, ab3531
EP1802Y	-	222–226 ⁱ (C-term)	R, IgG	Novus, NB110-57436
AB5058	-	79-97 ^m (OPR, CC2)	G, IgG	Merck, AB5058
H-8	-	N/A	M, IgG2a	SC, Sc-393165
G-12	-	N/A	M, IgG1	SC, Sc-398451
Pri-917	-	217–226 ⁿ (C-term)	M, IgG1	Spi, AO329
PrP 27-30	-	N/A	G, IgG	Fitzgerald, 20-PG73

1248 [†]Monospecific: An anti-PrP antibody is defined monospecific, if no residual signal (off-target binding)
 1249 is detected in *Prnp*-ablated cells. Antibodies with minor off-target effects are denoted +/-.

1250 [§]Abbreviation of PrP domains: N-term: N-terminus; OPR: octapeptide repeat region; CC2: charge
 1251 cluster 2; HR: hydrophobic domain; H1: helix 1; H2: helix 2; C-term: C-terminus.

1252 ^{*†}Hosts: M = mouse, R = rabbit, G = goat

1253 ^{*†}Vendors: SC: Santa Cruz Biotechnology, MRC: MRC Prion Unit, Sigma: Sigma Aldrich, Cayman:
 1254 Cayman Chemicals, Novus: Novus Biologicals, Spi: Spi Bio, TSC RC: TSE Resources Centre
 1255 (University of Edinburgh, UK).

1256 N/A: not applicable

1257 ^aLe et al., 2000⁶³; ^bLauren et al., 2009⁶⁴; ^cAntonyuk et al., 2009⁶⁵; ^dPan et al., 2004⁶⁶; ^eKang et al.,
 1258 2013⁶⁷; ^fZanusso et al., 1998⁶⁸; ^gSilva et al., 2012⁶⁹; ^hKatorcha et al., 2014⁷⁰; ⁱFaris et al., 2017⁷¹; ^m
 1259 Sauer et al., 1999⁷²; ⁿDemart et al., 1999⁷³

1260

1261 **Table S1: Validating the target specificity of anti-PrP antibodies using *Prnp* knockout**
 1262 **cells.** Anti-PrP antibodies were validated following genetic deletion of *Prnp* from N2a cells
 1263 using CRISPR-Cas9 (see Methods and Fig. S1A). To validate antibody specificity, fixed and
 1264 permeabilised N2a *Prnp*^{-/-} (ko) and N2a *Prnp*^{+/+} (wild-type) cells were incubated with anti-PrP
 1265 overnight. Cells were then washed twice with PBS and incubated with AF488-conjugated
 1266 secondary antibody. Residual fluorescence in *Prnp*^{-/-} N2a cells indicates off-target binding,
 1267 while complete abrogation of fluorescence confirms the mono-specificity of mAbs.

1268

anti-PrP mAb	Cellular Compartment	Mean fluorescence intensity \pm SEM [voxels/ μm^2]* 10^{-5}		T-test	Ratio \int MFI (infected/uninfected) \pm SEM
		Uninfected	Infected		
6D11	\ddagger PM	5.9 \pm 1.0	82.7 \pm 5.6	3.9 x 10 ⁻⁴	14 \pm 3
	*Peri	6.2 \pm 1.4	160.0 \pm 14.9	1.2 x 10 ⁻⁷	27 \pm 8
	$\#$ ECM	3.9 \pm 1.0	114.1 \pm 6.6	5.6 x 10 ⁻⁶	29 \pm 4
5B2	PM	4.9 \pm 0.4	65.2 \pm 6.1	4.4 x 10 ⁻¹³	13 \pm 2
	Peri	3.9 \pm 0.5	4.2 \pm 7.9	0.8	1 \pm 1
	ECM	5.0 \pm 0.4	119.0 \pm 6.5	3.8 x 10 ⁻¹²	23 \pm 2
Saf32	PM	22.3 \pm 1.0	75.9 \pm 4.1	2.4 x 10 ⁻¹⁰	3 \pm 0
	Peri	7.6 \pm 0.9	51.9 \pm 5.0	1.3 x 10 ⁻³	7 \pm 2
	ECM	10.0 \pm 3.7	117.5 \pm 3.4	2.3 x 10 ⁻¹⁰	12 \pm 1
ICSM18	PM	27.0 \pm 1.7	47.9 \pm 4.1	0.2	2 \pm 1
	Peri	13.6 \pm 6.0	36.8 \pm 3.4	6.9 x 10 ⁻³	3 \pm 1
	ECM	11.8 \pm 1.7	99.9 \pm 7.4	8.0 x 10 ⁻³	8 \pm 1
8H4	PM	29.4 \pm 2.1	60.4 \pm 3.7	1.5 x 10 ⁻⁸	2 \pm 0
	Peri	5.7 \pm 1.0	125.3 \pm 17.7	3.6 x 10 ⁻⁴	22 \pm 5
	ECM	12.7 \pm 1.3	66.9 \pm 2.3	1.5 x 10 ⁻⁸	5 \pm 0

1269 \ddagger PM: Plasma membrane; *Peri: Perinuclear region; $\#$ ECM: Extracellular matrix; \int MFI: Mean
1270 fluorescence intensity

1271 **Table S2: Voxel-based fluorescence intensities of anti-PrP antibodies for cellular**
1272 **compartments where PrP^d deposits.** Uninfected and prion-infected S7 cells were grown in
1273 OFCS for 4 days. Cells were then fixed with formalin (3.7%) for 12 min, followed by a 1 min
1274 and 10 min treatment with acetone and GTC (3.5M), respectively. After thorough washing
1275 with PBS, cells were labelled for 12 h with anti-PrP antibodies 6D11, 5B2, Saf32, ICSM18
1276 and 8H4. After washing with PBS, cells were labelled for 12 h with a Jackson Affinipure anti-
1277 M IgG (H+L) AF488 antibody and DAPI. Fluorescence intensities were set for the antibody
1278 with highest fluorescence intensities (6D11 in infected cells), using range indicator and kept
1279 the same for all other antibodies. Statistical significance was assessed by Student's T-test.

1280

Inhibitor	Concentration	Cytotoxicity [% of control]	Toxicity above threshold
Bafilomycin A1	24 nM	21.0	Yes
	12 nM	8.8	No
	6 nM	4.4	No
NH ₄ Cl	32 mM	25.0	Yes
	16 mM	1.4	No
	8 mM	0.8	No
Dynasore	40 μM	17.5	Yes
	20 μM	0.0	No
	10 μM	0.0	No
Dynole	5 μM	10.8	Yes
	2.5 μM	0.0	No
	1.25 μM	0.0	No
Pitstop 2	10 μM	12.5	Yes
	5 μM	7.5	No
	2.5 μM	3.2	No
Cytochalasin D	50 nM	0.8	No
	5 nM	2.0	No
	0.5 nM	7.1	No
Amiloride	40 μM	5.4	No
	20 μM	0.0	No
	10 μM	0.0	No
Vacuolin	5 μM	1.9	No
	2.5 μM	0.0	No
	1.25 μM	0.0	No
EGA	10 μM	2.3	No
	5 μM	1.6	No
	2.5 μM	3.5	No
Golgicide	20 μM	0.0	No
	10 μM	0.0	No
	5 μM	0.0	No
mβCD	4 mM	51.2	Yes
	2 mM	3.2	No
	1 mM	0.0	No
Retro-2	10 μM	8.0	No
	5 μM	2.3	No
	2.5 μM	0.2	No

1281 **Table S3: Toxic threshold levels of small molecule inhibitors**

1282 The cytotoxicity of small molecule inhibitors was assessed by measuring ATP levels by
1283 Luminescent Cell Viability Assay (Cell Titre Glo, Promega). Cells were plated out at a
1284 concentration of 5×10^4 cells per ml OFCS. Serially diluted inhibitors were added 16 h after
1285 plating. To take experimental variation into account, cytotoxic effects were scored positive,
1286 when a threshold of 10% was exceeded, when compared to mock controls.

Inhibitor	Concentration	Fold Change	T-test
Bafilomycin A1	100 nM	0.96	5.5×10^{-1}
	10 nM	0.90	3.6×10^{-1}
	1 nM	0.99	8.6×10^{-1}
	100 pM	1.00	9.1×10^{-1}
NH ₄ Cl	16 mM	0.99	8.8×10^{-1}
	8 mM	0.86	1.2×10^{-1}
	4 mM	0.93	0.9×10^{-1}
	2 mM	1.05	5.0×10^{-1}
Dynasore	5 μM	0.12	1.8×10^{-17}
	2.5 μM	0.11	8.0×10^{-17}
	1.25 μM	0.12	1.2×10^{-16}
	0.6 μM	0.16	5.9×10^{-16}
Dynole	2.5 μM	0.03	7.9×10^{-17}
	1.25 μM	0.26	2.0×10^{-12}
	0.6 μM	0.63	6.2×10^{-5}
	0.3 μM	0.92	3.5×10^{-1}
Pitstop 2	2.5 μM	1.24	1.0×10^{-1}
	1.25 μM	1.22	8.0×10^{-2}
	0.6 μM	1.11	3.2×10^{-1}
	0.3 μM	1.29	7.0×10^{-2}
Cytochalasin D	40 nM	0.60	8.0×10^{-11}
	20 nM	0.71	1.6×10^{-6}
	10 nM	0.77	1.6×10^{-6}
	5 nM	0.84	4.3×10^{-4}
Amiloride	20 μM	0.87	8.4×10^{-5}
	10 μM	0.90	4.7×10^{-4}
	5 μM	0.91	8.4×10^{-4}
	2.5 μM	0.93	6.3×10^{-2}
Vacuolin	5 μM	0.16	3.2×10^{-11}
	2.5 μM	0.19	8.4×10^{-11}
	1.25 μM	0.51	2.4×10^{-5}
	0.625 μM	0.74	1.2×10^{-2}
EGA	5 μM	0.37	3.6×10^{-14}
	2.5 μM	0.63	4.1×10^{-3}
	1.25 μM	0.93	4.4×10^{-1}
	0.625 μM	1.26	9.7×10^{-2}
Golgicide	5 μM	0.33	8.2×10^{-4}
	2.5 μM	0.76	1.5×10^{-1}
	1.25 μM	0.95	7.8×10^{-1}
	0.625 μM	1.21	3.7×10^{-1}
mβCD	2 mM	0.14	1.8×10^{-18}
	1 mM	0.40	8.2×10^{-11}
	0.8 mM	0.64	2.7×10^{-7}
	0.6 mM	0.80	6.2×10^{-5}
	0.4 mM	0.96	5.5×10^{-1}

1287

1288 **Table S4: Effect of small inhibitory molecules on the cellular prion steady state levels**

1289 Effects of small molecule inhibitors on the prion steady state levels were determined by
1290 SCA. Stock solutions of inhibitors were prepared in DMSO with the exception of NH₄Cl. To
1291 determine effects of small molecule inhibitors on prion steady state levels, 300 µl aliquots of
1292 chronically infected iS7 cells were plated into wells of 96-well plates at a concentration of 5 x
1293 10⁴ cells per ml OFCS. After 16 hours, cells were incubated with serially diluted inhibitors.
1294 After 3 days, cells were resuspended, diluted 1:10 in PBS and 100 µl of the cell suspension
1295 was transferred onto ELISPOT plates (Cat#. MSIPN4550, Merck Millipore Ltd, Tullagreen,
1296 Ireland) and prion titres were determined. Data represent fold change values, compared to
1297 mock (DMSO) treatment of at least three independent experiments.

1298

Control gene	Gene	Gene name	NCBI gene ID	Knockdown [%]
ActB	Prnp	Prion protein	19122	86.0 ± 3.6
	Clta	Clathrin, light polypeptide	12757	97.5 ± 0.9
	Cdc42	cell division cycle 42	12540	96.6 ± 2.1
	Dnm1	Dynamin 1	13429	95.4 ± 1.3
	Dnm2	Dynamin 2	13430	90.0 ± 0.1
	Rhoa	Ras homolog family member A	11848	95.3 ± 4.7
	Arf1	ADP-ribosylation factor 1	11840	42.3 ± 7.1
	Arf6	ADP-ribosylation factor 6	11845	44.6 ± 2.8
	Cav1	Caveolin 1	12389	N/A
Gapdh	Prnp	Prion protein	19122	84.2 ± 4.6
	Clta	Clathrin, light polypeptide	12757	97.8 ± 0.2
	Cdc42	cell division cycle 42	12540	96.5 ± 2.7
	Dnm1	Dynamin 1	13429	95.01 ± 0.9
	Dnm2	Dynamin 2	13430	89.4 ± 0.9
	Rhoa	Ras homolog family member A	11848	94.9 ± 2.3
	Arf1	ADP-ribosylation factor 1	11840	37.0 ± 2.6
	Arf6	ADP-ribosylation factor 6	11845	56.4 ± 4.2
	Cav1	Caveolin 1	12389	N/A

1300 N/A: not applicable: gene not expressed in S7 cells

1301 **Table S5: Efficacy of gene silencing by real-time quantitative PCR**

1302 Levels of gene expression following transcriptional silencing were determined by real-time
1303 quantitative PCR (RT-qPCR). Complementary DNA (cDNA) was synthesised with
1304 QuantiTect reverse transcription kit (Qiagen, Manchester, UK) using 500 ng of total RNA. All
1305 RT-qPCR reactions were carried out using a QuantStudio 12K Flex (Applied Biosystems,
1306 Cheshire, UK) with the following cycling parameters: 50°C, 2 mins; 94°C, 15 min; 40 cycles
1307 at 94°C, 15 sec; 60°C, 1 min. Samples were set up in triplicates in 10 µl reactions containing
1308 QuantiTect SYBR Green (Qiagen), 1x QuantiTect customised Primer Assay (lyophilized in
1309 TE, pH 8.0), 25 ng of cDNA made to a final volume with ddH₂O. Gapdh and Actb were used
1310 as endogenous controls for normalising target gene expression levels. Data acquisition of
1311 the fluorescent signal was performed at the end of the run to assess the expression of
1312 mRNA by evaluating threshold cycle (CT) values. Double delta CT calculations were
1313 measured as logarithm and then converted to fold change after untreated control levels were
1314 subtracted from target levels.

1315

1316

Inoculum	Time after infection	Cellular distribution of <i>de novo</i> myc PrP [% of positive cells]		
		[†] <i>Peri</i>	[#] <i>PM</i>	<i>Peri & PM</i>
RML	2 min	45.0 ± 4.4	40.3 ± 8.6	9.0 ± 8.7
	15 min	14.0 ± 13.9	62.7 ± 28.9	19.0 ± 22.0
Exosomes	2 min	55.0 ± 7.2	29.3 ± 16.9	23.3 ± 13.5
	15 min	40.0 ± 5.2	36.7 ± 15.8	25.3 ± 6.8

1317 †Peri: perinuclear; #PM: plasma membrane

1318 **Table S6: Identification of the cellular sites of *de novo* PrP conversion**

1319 The cellular distribution of *de novo* myc PrP in myc PrP/6D11 double-positive G70 PrP-
1320 expressing cells at 2 min and 15 min after infection with RML and exosomes was scored by
1321 three investigators. Data represents the cellular locations of *de novo* PrP in percent of the
1322 total positive cells scored. At least 50 myc PrP^d positive cells were analysed per condition.